

AD-A012 776

NEW TAPERED COMPOSITE SPAR DESIGN

Edward C. Poncia, et al

United Technologies Corporation

Prepared for:

Army Air Mobility Research and Development  
Laboratory

June 1975

DISTRIBUTED BY:

**NTIS**

National Technical Information Service  
U. S. DEPARTMENT OF COMMERCE

USAAMRDL-TR-75-17



217055

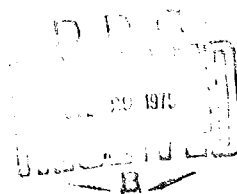
**NEW TAPERED COMPOSITE SPAR DESIGN**

ADA012776

Sikorsky Aircraft  
Division of United Technologies Corporation  
Stratford, Conn. 06602

June 1975

Final Report



Approved for public release;  
distribution unlimited.

Prepared for

EUSTIS DIRECTORATE  
U. S. ARMY AIR MOBILITY RESEARCH AND DEVELOPMENT LABORATORY  
Fort Eustis, Va. 23604

Reproduced by  
NATIONAL TECHNICAL  
INFORMATION SERVICE  
US Department of Commerce  
Springfield, VA 22151

UNCLASSIFIED

SECURITY CLASSIFICATION OF THIS PAGE (When Data Entered)

REPORT DOCUMENTATION PAGE		READ INSTRUCTIONS BEFORE COMPLETING FORM
1. REPORT NUMBER USAAMRDL-TR-75-17	2. SOVT ACCESSION NO.	3. RECIPIENT'S CATALOG NUMBER
4. TITLE (and Subtitle) NEW TAPERED COMPOSITE SPAR DESIGN		5. TYPE OF REPORT & PERIOD COVERED FINAL
		6. PERFORMING ORG. REPORT NUMBER
7. AUTHOR(s) EDWARD C. PONCIA TIMOTHY J. KRAUSS GEORGE H. STAAB		8. CONTRACT OR GRANT NUMBER(s) DAAJ02-74-C-0049
9. PERFORMING ORGANIZATION NAME AND ADDRESS SIKORSKY AIRCRAFT DIVISION OF UNITED TECHNOLOGIES CORPORATION STRATFORD, CONNECTICUT 06602		10. PROGRAM ELEMENT, PROJECT, TASK AREA & WORK UNIT NUMBERS 62208A 1F262208AH90 02 008 EK
11. CONTROLLING OFFICE NAME AND ADDRESS EUSTIS DIRECTORATE U.S. ARMY AIR MOBILITY RESEARCH AND DEVELOPMENT LABORATORY, FORT EUSTIS, VIRGINIA 23604		12. REPORT DATE June 1975
		13. NUMBER OF PAGES 119
14. MONITORING AGENCY NAME & ADDRESS (if different from Controlling Office)		15. SECURITY CLASS. (of this report) UNCLASSIFIED
		15a. DECLASSIFICATION/DOWNGRADING SCHEDULE
16. DISTRIBUTION STATEMENT (of this Report) Approved for public release; distribution unlimited.		
17. DISTRIBUTION STATEMENT (of the abstract entered in Block 20, if different from Report)		
18. SUPPLEMENTARY NOTES		
19. KEY WORDS (Continue on reverse side if necessary and identify by block number) HELICOPTERS, ROTOR BLADES (ROTARY WINGS), FILAMENT WOUND CONSTRUCTION FIBER ORIENTATION, PRODUCTION COST ANALYSIS, TAPERED SPAR		
20. ABSTRACT (Continue on reverse side if necessary and identify by block number) The purpose of this study was to design and evaluate a filament winding approach to the fabrication of a spar which tapered in planform and thickness. A cost and weight comparison was made with a conventional titanium spar design and an alternative composite design. The design included the integration of a suitable root end retention fitting.		

DD FORM 1 JAN 73 1473 EDITION OF 1 NOV 65 IS OBSOLETE

UNCLASSIFIED  
SECURITY CLASSIFICATION OF THIS PAGE (When Data Entered)

COPIES SUBJECT TO CHANGE

## SUMMARY

This report presents results of a design study of a tapered composite main rotor blade spar for the ABC<sup>TM</sup> helicopter. The objective of the study was to design and evaluate a filament winding approach on a spar which tapered in planform and thickness. The study included a production cost comparison with an alternative approach to a composite spar and a conventional titanium spar as used on the ABC<sup>TM</sup> demonstrator.

The study was limited to the evaluation of the production of a filament-wound spar including the integration of a root end retention fitting. It did not include an evaluation of reliability and maintainability.

The production cost comparison demonstrated the advantages of both composite designs over the conventional design. The high cost of the conventional design is due to the limited choices available for fabricating a heavy-walled titanium spar.

There are features in the filament-wound design which have not been demonstrated by fabrication but are considered to be within the state of the art; namely, the integration of the root end fitting and the terminations of the filament plies which are necessary to achieve a tapered planform. The integration of the root end fitting is a high risk area.

The filament-wound design produced a weight savings of 37 pounds as compared to the titanium spar blade with no significant change in the dynamic characteristics affecting rotor control.

## PREFACE

This design study for a tapered composite main rotor blade spar was performed under Contract DAAJ02-74-C-0049 with the Eustis Directorate, U. S. Army Air Mobility Research and Development Laboratory, Ft. Eustis, Virginia, and was under the general technical direction of Mr. James P. Waller of the Technology Applications Division of USAAMRDL.

Sikorsky's principal participants were Timothy A. Krauss and George H. Staab of the Rotor System Section. Edward C. Poncia, also from the Rotor System Section, was the Team Task Manager. The program was under the general supervision of Peter Arcidiacono, Rotor System Section Head.

Fiber Science Inc. of Gardena, California, was retained as consultant on the filament-wound design and assisted in the selection of materials in addition to providing guidance on the optimization of the application of filament winding.

TABLE OF CONTENTS

	<u>Page</u>
SUMMARY . . . . .	1
PREFACE . . . . .	2
LIST OF ILLUSTRATIONS . . . . .	5
LIST OF TABLES . . . . .	9
INTRODUCTION . . . . .	10
DEVELOPMENT OF METHODOLOGY AND DESIGN CONFIGURATION . . . . .	11
Program Approach . . . . .	11
Design Approach and Methodology . . . . .	11
Trade-off Methodology . . . . .	12
Materials Selection . . . . .	13
Manufacturing Processes . . . . .	13
DESIGN CONFIGURATIONS . . . . .	15
Filament Winding Design . . . . .	15
Twin-beam Design . . . . .	16
Conventional Design . . . . .	29
ANALYSIS OF FILAMENT WINDING DESIGN . . . . .	30
Selection of Fiber Orientation . . . . .	30
Determination of Spar Geometrical Shape . . . . .	30
Determination of Detail Lay-up Variation . . . . .	33
Alternate Windin <sup>g</sup> Investigation . . . . .	44
Rotor Blade Physical Properties . . . . .	45
Dynamic Characteristics . . . . .	58
Loads Development . . . . .	62

TABLE OF CONTENTS

	<u>Page</u>
Blade Stress Analysis . . . . .	62
Root End Attachment . . . . .	71
Analysis of Bond Joint . . . . .	74
Titanium Backup Structure . . . . .	88
LAP SHEAR TESTS. . . . .	95
TRADE-OFF STUDIES . . . . .	100
Filament-Wound Spar Design Costs . . . . .	100
Twin-beam Design Costs . . . . .	101
Demonstrator Blade Costs . . . . .	103
Summary of Cost Trade-offs . . . . .	105
Spar Weight Summary . . . . .	105
CONCLUSIONS. . . . .	107
RECOMMENDATIONS . . . . .	109
REFERENCE . . . . .	110
LIST OF SYMBOLS . . . . .	111

LIST OF ILLUSTRATIONS

<u>Figure</u>		<u>Page</u>
1	Tensile and Shear Modulus Comparison for Thornel 300 and AS Graphite . . . . .	14
2	ABC Filament-wound Composite Spar Main Rotor Blade . . . . .	17
3	ABC Root End Fitting, Main Rotor Blade . . . . .	19
4	ABC Composite Main Rotor Blade Twin-beam Construction. . . . .	21
5	Lower Half of Twin-beam Inboard Clamshell Tool . . . . .	24
6	Twin-Beam Construction - Machining of Mid-Plane after Curing of Blade Half . . . . .	25
7	ABC Demonstrator Titanium Spar, Main Rotor Blade . . . . .	27
8	Determination of Spar Shape of Filament-Wound Tube during Forming . . . . .	31
9	Variation of Outside Diameter of Round Tube Prior to Forming Filament-Wound Spar Shape . . . . .	32
10	Tensile and Shear Modulus for Varying Percentages of $\pm 15^\circ$ and $\pm 45^\circ$ Plies of Thornel 300 . . . . .	34
11	Spar Station 30 Stiffness Ratio vs Spar Thickness for Constant Winding Angle. . . . .	35
12	Spar Station 45 Stiffness Ratio vs Spar Thickness for Constant Winding Angle . . . . .	36
13	Spar Station 65 Stiffness Ratio vs Spar Thickness for Constant Winding Angle . . . . .	37
14	Spar Station 95 Stiffness Ratio vs Spar Thickness for Constant Winding Angle . . . . .	38
15	Spar Station 135 Stiffness Ratio vs Spar Thickness for Constant Winding Angle . . . . .	39
16	Spar Station 155 Stiffness Ratio vs Spar Thickness for Constant Winding Angle . . . . .	40
17	Spar Station 195 Stiffness Ratio vs Spar Thickness for Constant Winding Angle . . . . .	41
18	Spar Station 30 Stiffness Ratio vs Spar Thickness for Variable Winding Angle . . . . .	46

LIST OF ILLUSTRATIONS

<u>Figure</u>		<u>Page</u>
19	Spar Station 45 Stiffness Ratio vs Spar Thickness for Variable Winding Angle . . . . .	47
20	Spar Station 65 Stiffness Ratio vs Spar Thickness for Variable Winding Angle . . . . .	48
21	Spar Station 95 Stiffness Ratio vs Spar Thickness for Variable Winding Angle . . . . .	49
22	Spar Station 135 Stiffness Ratio vs Spar Thickness for Variable Winding Angle . . . . .	50
23	Spar Station 155 Stiffness Ratio vs Spar Thickness for Variable Winding Angle . . . . .	51
24	Spar Station 195 Stiffness Ratio vs Spar Thickness for Variable Winding Angle . . . . .	52
25	Blade Weight Comparison. . . . .	53
26	Blade Flapwise Stiffness Comparison of Demonstrator and Composite Blades . . . . .	54
27	Blade Edgewise Stiffness Comparison of Demonstrator and Composite Blades . . . . .	55
28	Blade Torsional Stiffness Comparison of Demonstrator and Composite Blades . . . . .	56
29	Composite Blade Axial Stiffness. . . . .	57
30	Demonstrator Blade Natural Frequency . . . . .	59
31	Composite Blade Natural Frequency. . . . .	60
32	Blade Vibratory Bending Moments . . . . .	63
33	Blade Torsional Moment . . . . .	64
34	Blade Centrifugal Force . . . . .	65
35	Blade Flapwise Static Moment . . . . .	66
36	Blade Edgewise Static Moment . . . . .	67
37	Notation Used for Strain Calculations . . . . .	68
38	Root End Attachment - Bolted Joint . . . . .	72

LIST OF ILLUSTRATIONS

<u>Figure</u>		<u>Page</u>
39	Root End Attachment - Bonded Joint . . . . .	72
40	Root End Attachment - Double-Bonded Tapered Cylinder . . . . .	73
41	Root End Attachment - Single-Bonded Tapered Cylinder . . . . .	73
42	Segments Used in Bond Joint Analysis . . . . .	75
43	Modeling of Structure for Bond Stress Study - Actual Structure . . . . .	76
44	Modeling of Structure for Bond Stress Study - Model Used for One-Dimensional Analysis . . . . .	76
45	Ratio of Bond Shear Stress Levels to Peak Bond Shear Stress for Various Tip Configurations . . . . .	78
46	Bond Shear Stress Comparison for Various Joint Lengths After Taper. . . . .	79
47	Finite-Element Model . . . . .	82
48	Correlation of Bond Shear Stress Levels for Finite- Element and Bonded Joint Analysis . . . . .	83
49	Bond Shear Stress for Various Incline Angles . . . . .	84
50	Model for Determining Hoop Winding . . . . .	85
51	Vibratory Axial Stress in Bonded Joint . . . . .	87
52	Theoretical Model of Joint for Stress Concentration Factor . . . . .	89
53	Theoretical Stress Concentration Factor for Titanium Fitting . . . . .	90
54	Flange Loading . . . . .	91
55	Relative Axial Stress Levels Along the Radius of the Bearing Retention Flange of Various Geometries . . . . .	92
56	Geometry of Lap Shear Specimens. . . . .	95
57	Testing of Lap Shear Specimens . . . . .	96
58	Bond Shear Stress for Lap Shear Tensile Test Model . . . . .	98

LIST OF ILLUSTRATIONS

<u>Figure</u>		<u>Page</u>
59	ABC to H-3 Size Comparison . . . . .	102
60	Spar Weight Distribution for Composite and Demonstrator Spars . . . . .	106

LIST OF TABLES

<u>Table</u>		<u>Page</u>
1	Thickness per Layer as Governed by Tube Diameter .	43
2	Achievable Spar Thickness. . . . .	44
3	Variation of E and G for Variable Winding Angle and Constant Thickness . . . . .	45
4	Properties of the Vibration Modes at Normal Rotor Speeds . . . . .	61
5	Blade Fatigue Strain Summary . . . . .	69
6	Blade Ultimate Strain Summary . . . . .	70
7	Configurations Investigated in Titanium Bearing Retention Flange Analysis . . . . .	93
8	Nonbonded Lap Shear Test Results . . . . .	99
9	Bonded Lap Shear Test Results. . . . .	99

## INTRODUCTION

Filament winding as a production process has long been established and used on a variety of components. Its application to a helicopter main rotor blade tapering in planform and thickness has not been developed. The requirements for a blade of this type exist on the ABC<sup>TM</sup>, which has counter-rotating blades and a high stiffness criterion. The selection of the ABC<sup>TM</sup> as the vehicle for which to develop a filament wound rotor blade spar was advantageous because of the existence of established design criteria and a metal spar solution for direct comparison. Also, the blade design incorporates a wide variation in geometry, allowing maximum assessment of the filament winding capability; the existing ABC<sup>TM</sup> aircraft provides for the potential of developing the blade to the final stages of flight testing.

The study was confined to the design of the spar, supported by some tests of specimens to determine bond allowables for the curing conditions applied to the root retention fitting integration. Cost comparisons were made to determine the cost effectiveness of the filament winding approach compared to other approaches. The other approaches used for comparison were

1. An alternative composite fabricated by a two half molding process.
2. The design used on the ABC<sup>TM</sup> demonstrator which used a titanium spar.

The report will first describe the three design approaches compared for cost effectiveness, including the manufacturing processes applied to each of these. The manufacturing processes include prototype fabrication and high production fabrication. The methodology in optimizing the filament winding design and a discussion on the risk areas are presented. The report also includes a recommended plan for subsequent research.

## DEVELOPMENT OF METHODOLOGY AND DESIGN CONFIGURATION

### PROGRAM APPROACH

Three alternative design approaches were compared to determine the cost effectiveness of the filament winding approach. The primary emphasis was placed upon an analysis of the design, manufacture and risks associated with filament winding a spar to the design requirements of the ABC<sup>TM</sup> main rotor blade. The design was confined to replacement of the ABC<sup>TM</sup> demonstrator titanium spar, taking advantage of composites to reduce weight and making design improvements within their capabilities. The ABC<sup>TM</sup> demonstrator helicopter was produced under Army contract DAAJ02-72-C-0020 to evaluate the performance of the counter rotating main rotor blade concept. The root end fitting design integrated into the composite design was based upon work previously conducted which showed that the pitch bearing design could be improved over the demonstrator configuration. The costs and weight changes associated with this variation were not included in the trade-off studies since they are applicable to all three design configurations equally.

### DESIGN APPROACH AND METHODOLOGY

The ABC<sup>TM</sup> concept involves forcing the rotor blades, in forward flight, to generate their full lift capability in the advancing portions of the rotor disk. This is unlike conventional rotor systems, in which the blades generate lift primarily in the fore and aft disk positions. The concept involves counter rotating rotors providing for two simultaneously advancing blades to balance the rotor rolling moment and a sufficiently small phase angle of the primary flapping mode to allow the advancing blade to lift.

Flapwise stiffness is also a primary requirement to prevent blade contact of blades on the closely stacked upper and lower rotors.

Both of these requirements are met on the ABC<sup>TM</sup> by providing blades cantilevered from the rotor hub with high inboard stiffness and highly tapered chord and thickness distribution. Thus in the design of the composite spar for the ABC<sup>TM</sup>, a primary consideration was that the blade flapwise stiffness was at least as great as the demonstrator blades and that the response phase angle of the first flapwise mode was approximately the same as the demonstrator insuring similar control characteristics.

The desired chordwise stiffness was to be higher than that on the demonstrator blades to move the first chordwise mode well above one-per-rev at normal rotor speed. Since the demonstrator blades had more than sufficient torsional stiffness, no restrictions were put on this quantity except that the stiffness was not permitted to fall below that of the demonstrator blades in the thin-soft tip region. Because of the higher fatigue strength allowables of the composite materials relative to titanium, the fatigue margins were easily achieved.

The blade aerodynamic contours were kept identical to the demonstrator blade; inboard of the airfoil cutoff, however, the spar tube has an increased diameter to mate with the improved pitch bearing system which is incorporated in this design. The twist distribution, radius, and tip speed were also kept identical to the prototype.

Sizing of the blade spar wall thickness distributions was accomplished by use of section property computer programs which are coupled with a cathode-ray tube interface system (CRT). The system allows the engineer to generate rotor blade section characteristics on line by providing instant interaction with the computer program. Bending-torsional stiffness relationships were derived as a function of thickness and ply lay-up percentage at a number of blade stations to design the spar.

Torsion and bending mode characteristics were derived from a 50 station free vibration computer program (Program Y172).

Derivation of aeroelastic loads for the flight spectrum was beyond the scope of this program. Fatigue loads were derived from calculated root end bending moments on the demonstrator blade. The spanwise moment distribution corresponding to the lowest flapwise and chordwise bending modes were used to determine the ratio of the moment at any blade station to root moment. From these ratios, spanwise distributions of bending moments were determined from the calculated root moments.

Critical ultimate loads were derived by a similar approach for flight loads; a ground loads computer program was used to derive the ultimate loads resulting from ground conditions.

Detail stress analysis of the root end retention fitting was accomplished using Sikorsky's bond joint computer program (Y004-B) and the United Aircraft two-dimensional finite-element computer program (F768).

#### TRADE-OFF METHODOLOGY

Background data on the ABC<sup>TM</sup> demonstrator titanium spar blade was collected together with the background data on the H-3 composite twin ocean design which is being developed under U. S. Navy Contract N00015-73-C-0319. This data was normalized to reflect the 1980 projected cost of materials and to a common baseline for labor cost per hour. The filament winding manufacturing process for the prototypes. Learning curve methods were applied to the three approaches to project production costs. The learning curves applied took into account the fact that the prototype fabrication in all cases would be modified to high production methods using equipment that would be expected to be available in the 1980 time frame. The slope of the learning curve was 85%.

## MATERIALS SELECTION

The materials selection was confined to the spar with no attempt to vary the general construction of the remainder of the blade. Skins and pockets were considered to remain basically the same construction as that used in the demonstrator blade. The material for filament winding a composite spar was chosen from three candidates, fiberglass, boron, and carbon. The objective of achieving weight savings eliminated fiberglass. Boron was considered to be high risk for the filament winding process under consideration, and project costs indicated that it would not be as cost effective as carbon. The carbon selected was Thornel 300 on the basis of its higher modulus and very slight cost difference to the AS graphites (see Figure 1). This material is also more compatible with the filament winding operations. The resin selection was restricted to a wet winding process with the necessary pot life. Two candidates were selected, one of which is a fully developed system; the second, which shows high promise, would be expected to be developed fully in the 1980 time frame. Pre-preg materials were not considered due to their relatively high cost compared to dry filament and wet resin systems. A survey of filament winding resins revealed that various manufacturers of filament winding have their own preferences based upon previous usage. The resins selected were based upon the experience of the filament winding consultants on this program.

## MANUFACTURING PROCESSES

The filament winding procedure considered for the prototype fabrication was based upon a wet winding process. The winding is made over an inflated mandrel which subsequently becomes the pressure bag for the cure cycle. At the completion of the winding, the spar is placed into a female die, pressure is applied to the inside of the winding mandrel and the cure cycle is performed after the die is closed.

The twin beam construction, which was the alternative composite design used to determine the cost effectiveness of the filament winding design, is fabricated by laying up pre-preg material into the two open halves of a female mold. After the two halves are cured, a machining operation trims the two parts flush to the split line of the female mold. The two halves are then bonded together.

The titanium demonstrator spar was fabricated by an extrusion operation followed by machining of both the inside and outside surfaces. The resulting tube was then hot formed in a female ceramic die.

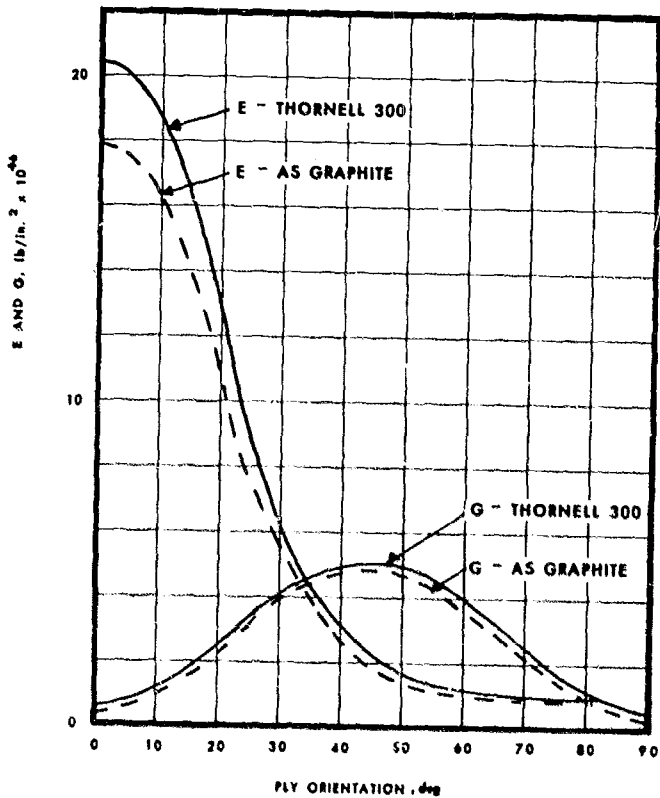


FIGURE 1. TENSILE AND SHEAR MODULUS COMPARISON FOR THORNELL 300 AND AS GRAPHITE.

## DESIGN CONFIGURATIONS

### FILAMENT WINDING DESIGN

The final version of the filament-wound configuration is shown in Figure 2. The Thornel 300 graphite filaments are wound with a mixture of  $\pm 15^\circ$  layers alternating with  $\pm 45^\circ$  layers in the ratio of 70% of  $\pm 15^\circ$  and 30% of  $\pm 45^\circ$ . The sequence of layers as shown in Figure 2 is approximately two layers of  $\pm 15^\circ$  alternated with one layer of  $\pm 45^\circ$ . The root end fitting, Figure 3, is integrated with the spar by positioning the fitting on the winding mandrel before the winding operation commences. Film adhesive is wrapped around the area of the fitting that is in contact with the winding. To obtain the required thickness on the tapered platform, layers of windings are terminated at staggered intervals along the span.

The epoxy resin system used in the wet winding process becomes a choice between a system that has been fully developed and an improved impact resistance system which has not been fully characterized at this time and requires improvements to the elevated temperature properties. The fully developed resin is APCO 2434/2347.

The blade contours are unchanged from the demonstrator blades. These comprise NACA63-2XXA(230) airfoil inboard to Station 135 and NACA 23012(64) airfoil outboard at Station 155 with a 20-inch transitional section between.

This design was developed taking into account the manufacturing limitations and capabilities of a post-formed geodesic filament winding process. The angle of  $\pm 15^\circ$  was selected as the closest that a geodesic filament winding process can approach  $0^\circ$  angle with economical manufacture. Low emphasis was placed upon limiting the design to only those operations which have been fully proven since previous attempts to fabricate this type of component have been limited. By placing low emphasis on restricting the design to proven capabilities, two of the features of this design introduce a high degree of hand work into the filament winding process for fabricating small quantities of prototype spars. One of these features is the terminations of plies along the span in order to maintain the required thickness. Each termination on the prototypes will require that the winding operation be interrupted to hand trim the laminate at the designated stations. An alternative method of achieving the terminations without interrupting the winding process was not considered for this design due to the weight penalty attached in the method. This procedure involved a gradual change of angle until the  $90^\circ$  angle was reached, at which point, the winding direction was reversed. This produces a distance of 4 feet and 6 inches respectively on the  $15^\circ$  and  $45^\circ$  winding layers which would not be considered optimum fiber orientation. The other feature producing hand work is the use of a pure geodesic winding into the area of the fitting for the  $\pm 15^\circ$  winding angle. This will require an interruption of the winding process to lock each tow at the end of a pass before the carriage can return. This operation is required to keep the filaments from slipping out of position. The limitations referred to exist on a general purpose

single carriage winding machine. It is reasonable to expect that these problems can be eliminated in a more complex piece of equipment that would be used for high production.

The design of the spar requires that the external contours be held to a close tolerance since this determines the accuracy of the final airfoil. After the spar is formed, the outer skin is directly attached to the spar in a manner that provides no tolerance adjustment to be made to the outside contour. To attain the required degree of accuracy, the final curing operation would necessarily be performed with a female die, with internal pressure being applied to the spar. This procedure provides for the buildup of tolerances, due to lamination variations, affecting the less critical inside contour. The final cure operation would be the same for two alternative approaches to the filament winding process: (1) winding over a circular shape and post forming and (2) winding over a finished spar shape. The filament winding consultant on this program expressed preference for (1).

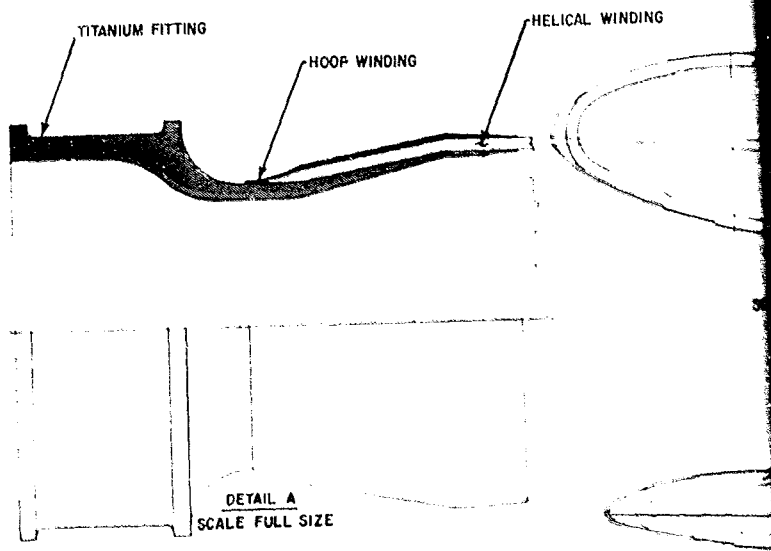
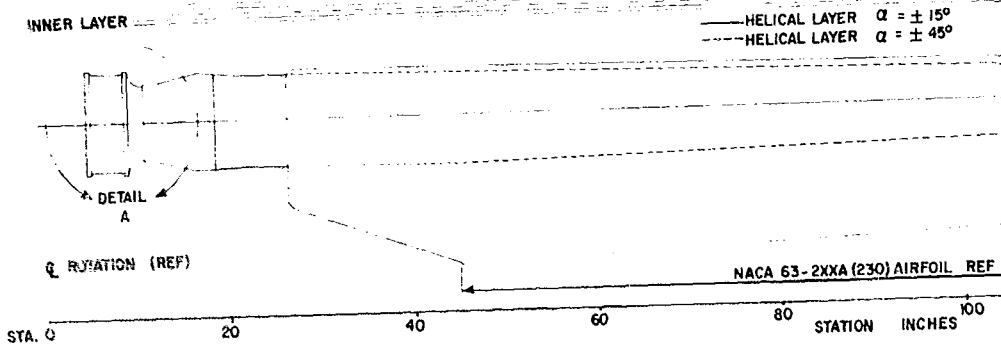
The risk areas of this design are:

- (a) Obtaining repeatability of the fiber and resin volume to the accuracy required to obtain the stiffness and mass properties tolerances necessary for a main rotor blade.
- (b) Maintaining a consistent degree of compaction in the matrix in the free-forming radii at the leading and trailing edges of the spar.
- (c) Development of the root end retention fitting integration with the filament winding.

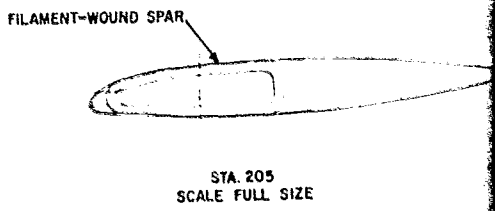
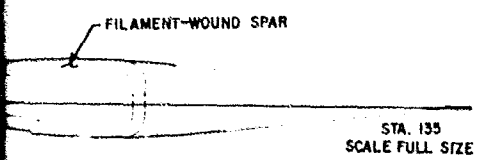
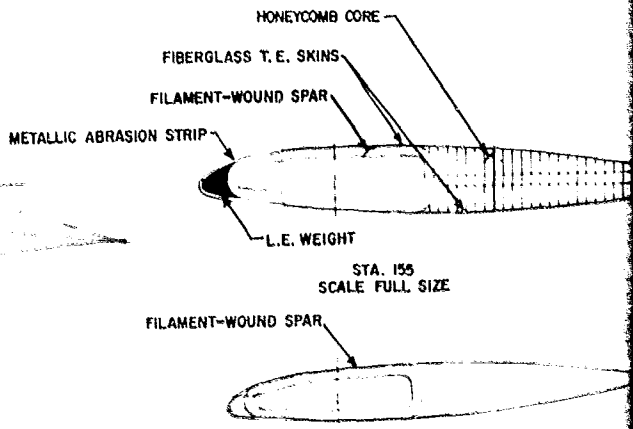
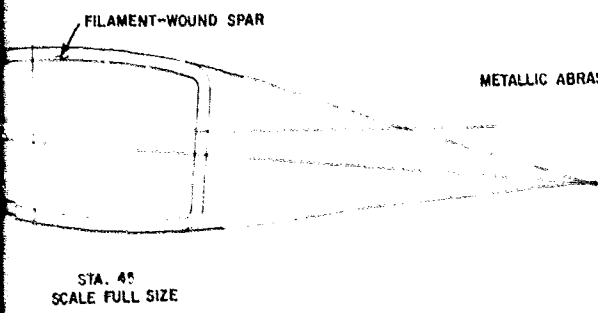
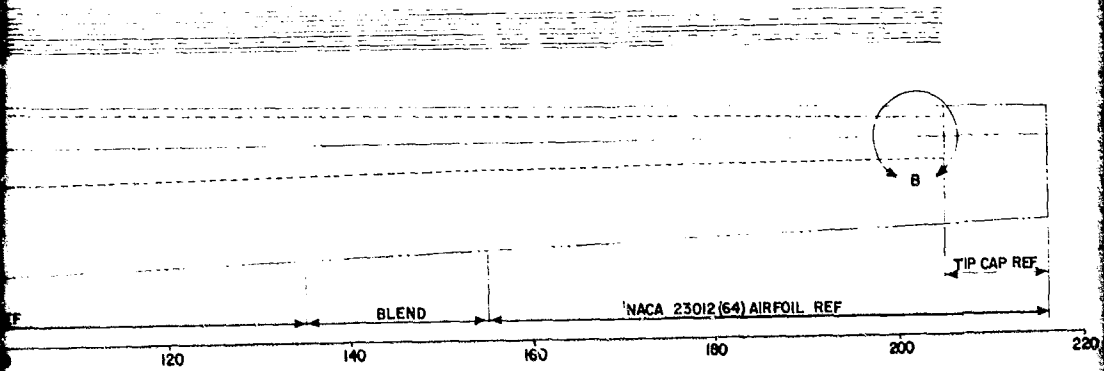
The risks described may all be minimized by development. The repeatability of fiber and resin volume would be expected to be obtained with high quality tooling and equipment development which were designed with recognition that this risk exists. The leading edge and trailing edge radii which are allowed to free-form inside the clamshell cavity could be controlled by a flexible insert in the tool to provide a reaction point sufficiently rigid to apply compaction but flexible enough to allow the radii to form without producing a kink in the fibers. The root end retention fitting selected for this design was chosen for its low weight potential. In the event that the integration of this design produced insurmountable problems, there are several other design options available.

#### TWIN BEAM DESIGN

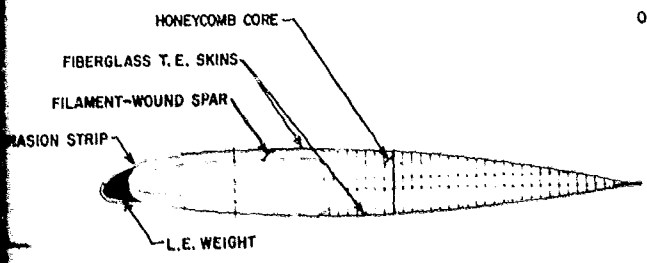
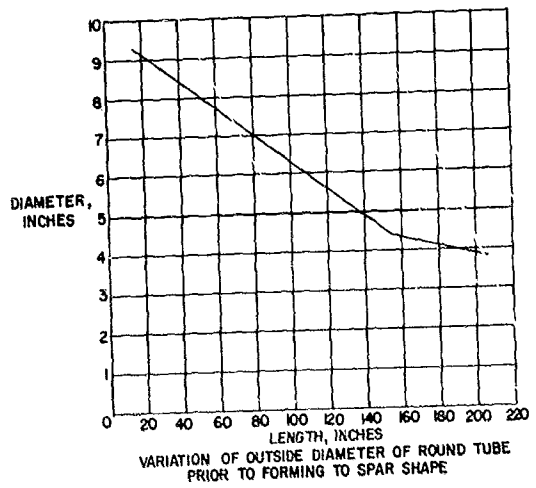
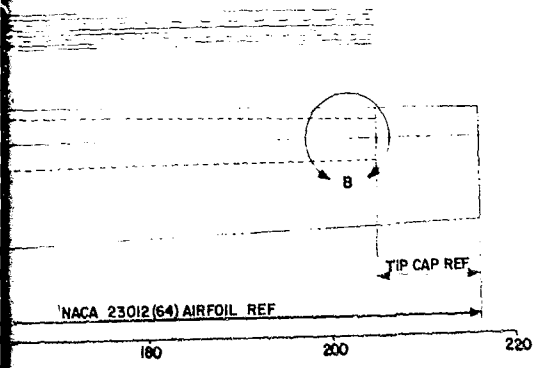
This design is an adaption of the H-3 composite blade which is currently being developed under a Navy contract. The configuration to the ABC<sup>TM</sup> geometry and requirements is shown in Figure 4. The design incorporates an outboard spar structure different from the filament-wound design and involves a unique fabrication approach. Outboard, the elliptical closed-section spar of the filament-wound design is replaced by two halves which are joined at the leading edge by a splice and are closed at the trailing



ABC FILAMENT-WOUND COMPOSITE SPAR, MAIN ROTOR BLADE.



← 5 IN. APPROX. →

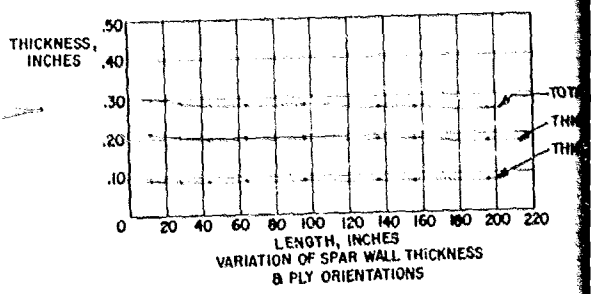


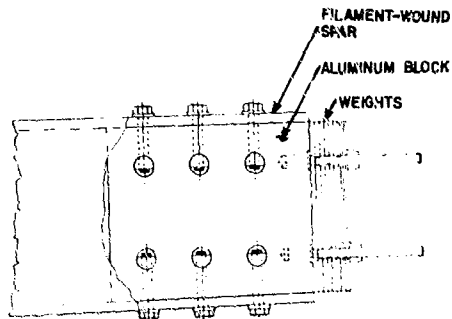
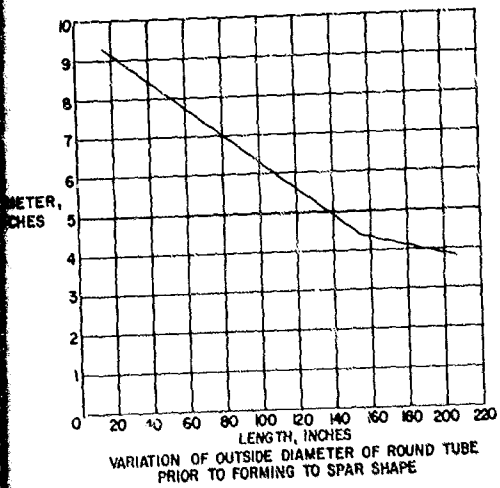
STA. 155  
SCALE FULL SIZE



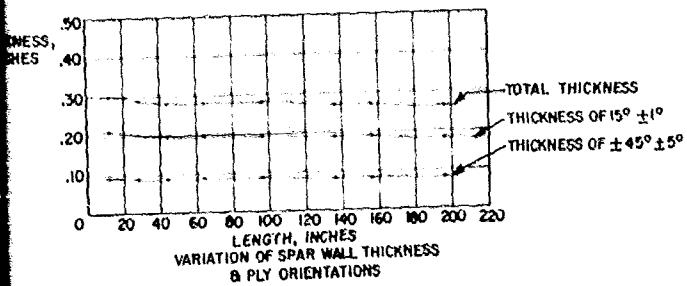
STA. 205  
SCALE FULL SIZE

← 5 IN. APPROX. →





← 5 IN. APPROX. →





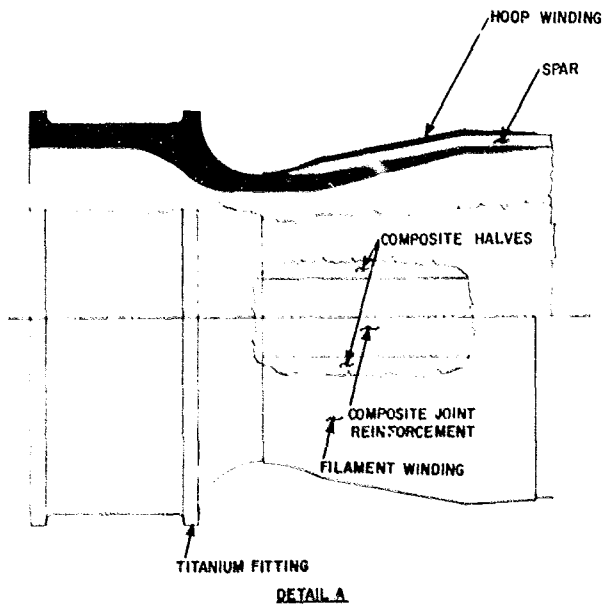
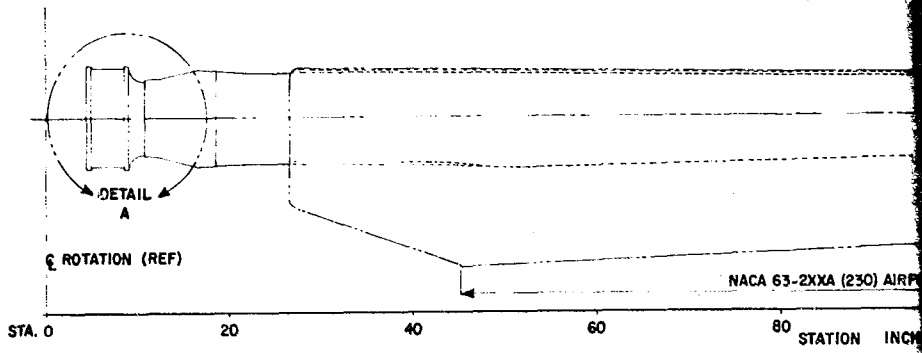


FIGURE 4. ABC COMPOSITE MAIN ROTOR BLADE, TWIN-BEAM CONSTRUCTION.

NACA 63-2XXA (230) AIRFOIL REF

BLEND

NACA 23012

80 STATION INCHES 100

120

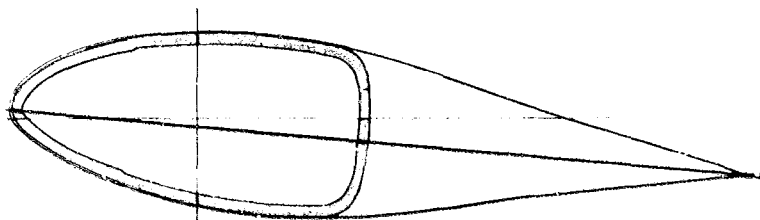
140

160

HOOP WINDING

SPAR

ALVES

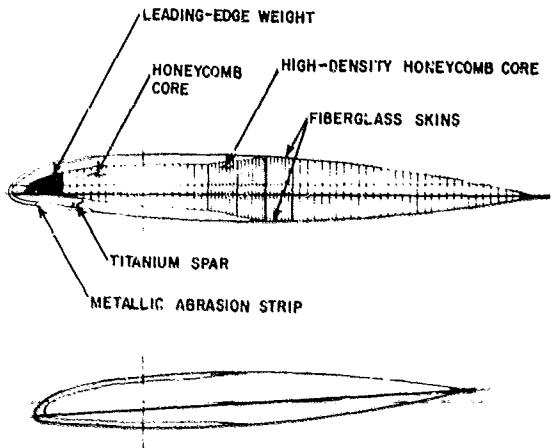
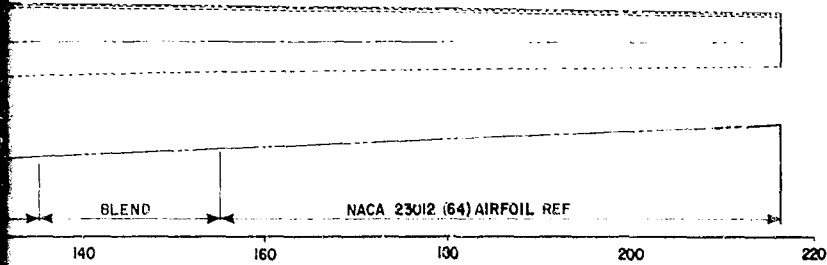


STA. 45  
SCALE FULL SIZE



STA. 135  
SCALE FULL SIZE

STRUCTION.



← 5 IN. APPROX. →

edge by a section of high-density honeycomb. Inboard, the C-shaped spar transitions into a closed elliptical shape resulting in a structure similar to the filament-wound spar. The integration of the root end fitting is accomplished by splicing the two half spars over the fitting, with a film adhesive between the spar and fitting, followed by hoop winding over the outside of the spar in the region of the fitting.

Figures 5 and 6 illustrate the essential operations of this manufacturing process. Two half molds representing the outside contour of the finished blade are used to lay up the skin, spar and core materials. Each half is then cured with pressure being applied to the open side of the half molds. After the curing, the core, skin and spar materials standing above the split line of the mold are machined away. Both halves of the blade are then brought together and bonded. Because both halves of the blade are laid-up in female molds and are machined to a flat surface at the bond line before being brought together, the finished blade has good contour control.

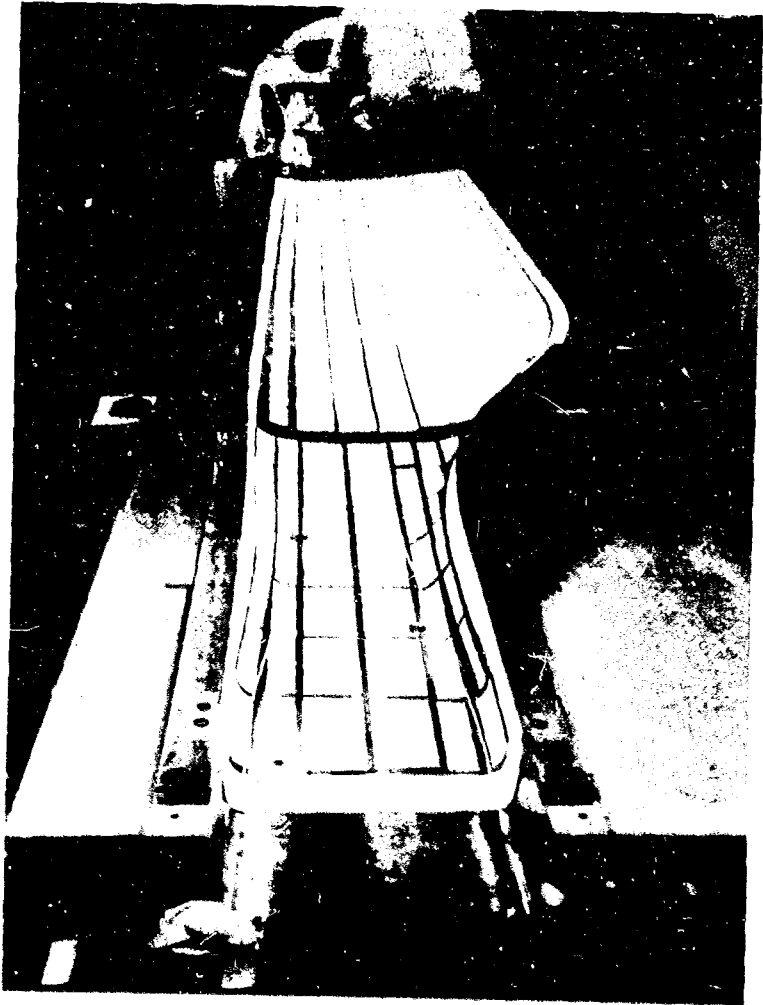
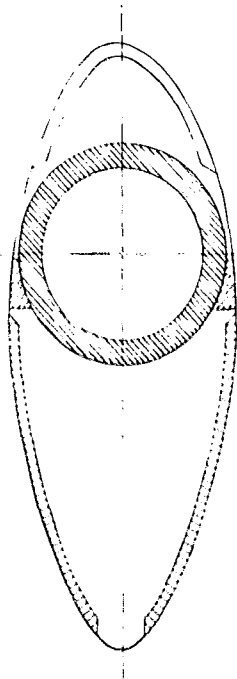
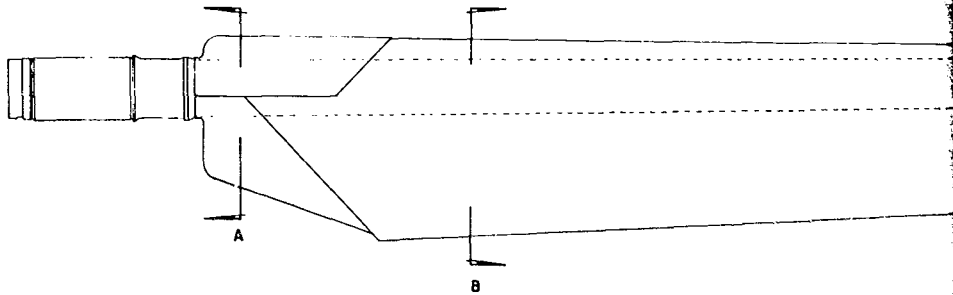


**FIGURE 5. LOWER HALF OF TWIN-BEAM INBOARD CLAMSHELL TOOL.**



FIGURE 6. TWIN-BEAM CONSTRUCTION - MACHINING OF MID-PLANE  
AFTER CURING OF BLADE HALF.



SECTION AA

FIGURE 7. ABC DEMONSTRATOR TITANIUM SPAR, MAIN ROTOR BLADE.

Preceding page blank

← 5 11

ABRASION STRIP

FOAM

TITANIUM SPAR

HONEYCOMB

FIBERGLASS SKIN

← 5 IN. APPROX. →

SECTION BB

### CONVENTIONAL DESIGN

Due to the high stiffness requirements of the ABC<sup>TM</sup> blade, the conventional or metal solution is a titanium spar (Figure 7). Some additional flatwise stiffness is obtained by strips of boron on the upper and lower surfaces of the spar. Nomex honeycomb core and fiberglass skins form the pocket areas as in the composite designs.

The thick-wall requirements in the titanium spar leave very few choices in the method of manufacture. The method used on the demonstrator blades comprised several expensive procedures. Starting with an extruded billet, the inside and outside surfaces were machined into a tapered wall round tube. After machining the round tube was hot creep formed between ceramic female dies to the finished shape including twist.

## ANALYSIS OF FILAMENT WINDING DESIGN

### SELECTION OF FIBER ORIENTATION

In the design of a composite rotor blade structure, normally the bending stiffness and strength are obtained primarily by spanwise fiber plies and torsional stiffness is achieved primarily by plies oriented at  $\pm 45^\circ$  to the span. Based on the recommendation of the filament winding consultants, the plies should not be less than  $\pm 15^\circ$  to the span in order to achieve optimum producibility. Thus, a combination of  $\pm 15^\circ$  and  $\pm 45^\circ$  windings was chosen for the design of the spar.

### DETERMINATION OF SPAR GEOMETRICAL SHAPE

The proposed filament winding technique involved winding the spar as a tapered circular cylinder and forming, after winding, into the desired geometry. The diameter of the cylinder was calculated with the aid of the aforementioned CRT computer analysis. The diameter of the root end configuration (which remains circular in the final formed shape) was sized to be compatible with the root end fitting, whose geometry was in turn governed by the pitch bearing diameter of the improved rotor hub. The clamshells in which the spar would be formed were shaped to yield final outboard blade airfoil contours identical to the demonstrator blade. The round spar was positioned in the open dies so that its center coincides with the blade pitch axis. During closing of the clamshell dies on the spar, the first point of contact between the die and the spar determined the distribution of material within the closed shape. Since the final spar periphery was fixed by the initial diameter, the chord of the spar was determined by the amount by which the diameter of the tube was flattened (see Figure 8). Using a trial and error process on the CRT, the diameter of the spar at Station 155 (inboard end of the 23012 airfoil region) was varied until the largest value that produced a sufficiently large leading-edge radius (for forming) was determined. A linear variation between the diameter at this station and the root diameter was assumed for simplicity in the internal mandrel. Intermediate stations were checked to insure that the leading-edge radii were acceptable. Finally, a diameter at the most outboard station of the spar was determined by the same process and a linear variation in diameter was assumed. The resulting variation of diameter with blade span is shown in Figure 9.

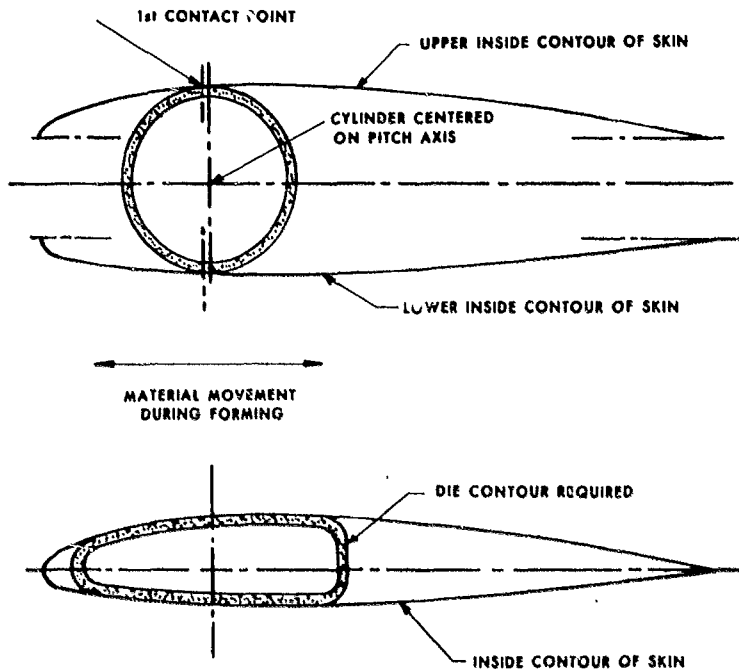


FIGURE 8. DETERMINATION OF SPAR SHAPE OF FILAMENT-WOUND TUBE DURING FORMING.

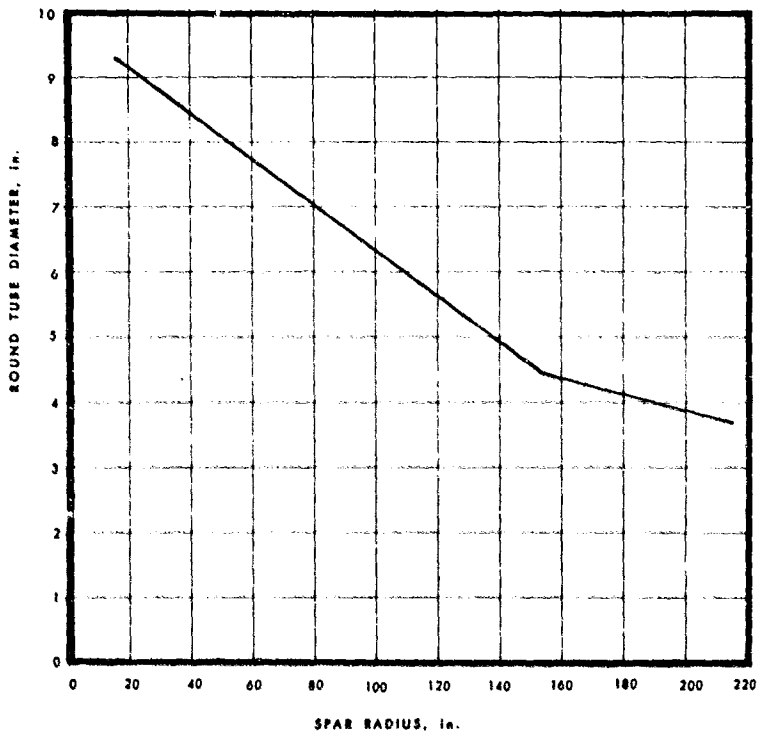


FIGURE 9. VARIATION OF OUTSIDE DIAMETER OF ROUND TUBE  
PRIOR TO FORMING FILAMENT-WOUND SPAR SHAPE.

#### DETERMINATION OF DETAIL LAY-UP VARIATION

Using the Sikorsky laminate analysis computer program (E952), the elastic moduli were calculated for Thornel 300 graphite epoxy material for various ratios of the  $\pm 15^\circ$  to the  $\pm 45^\circ$  laminates. The results are presented in Figure 10.

Using the CRT analysis, spar section properties were calculated at a number of stations along the span for various thicknesses and various lay-up ratios. At each station investigated, relationships were developed between the spar stiffness and both the spar thickness and the lay-up ratio.

To relate the stiffness trends to the demonstrator titanium spar, the following nondimensional parameters were defined:

$$\alpha_x = \frac{EI_{xx \text{ composite spar}}}{EI_{xx \text{ demonstrator spar}}} \quad (1)$$

$$\alpha_y = \frac{GJ_{\text{composite spar}}}{GJ_{\text{demonstrator spar}}} \quad (2)$$

Maps of these parameters as a function of thickness and lay-up ratio were developed at each selected station and are presented in Figures 11 through 17.

To facilitate the winding operation, it is desirable to maintain a constant ratio of the  $\pm 15^\circ$  plies to the  $\pm 45^\circ$  plies over the total span. To meet the blade clearance criterion, it was decided to match the flapwise stiffness of the titanium spar as closely as possible. The procedure used to define the spar winding diameter resulted in a spar with considerably more chordwise depth than the demonstrator; thus, matching the flapwise stiffness would result in a spar of increased edgewise stiffness, which was desired. Torsional stiffness was permitted to deviate from the demonstrator values except in the tip area where minimum acceptable values exist as previously mentioned.

At  $\alpha_x = 1.0$ , for inboard stations, the torsional stiffness is less than the demonstrator; outboard it is greater than the demonstrator, which is a perfectly suitable situation. Thus, emphasis could be placed on  $\alpha_x$  alone since the other parameters follow in the desired direction. Many combinations of thickness and percentage ply lay-up appear to meet the stiffness criterion.

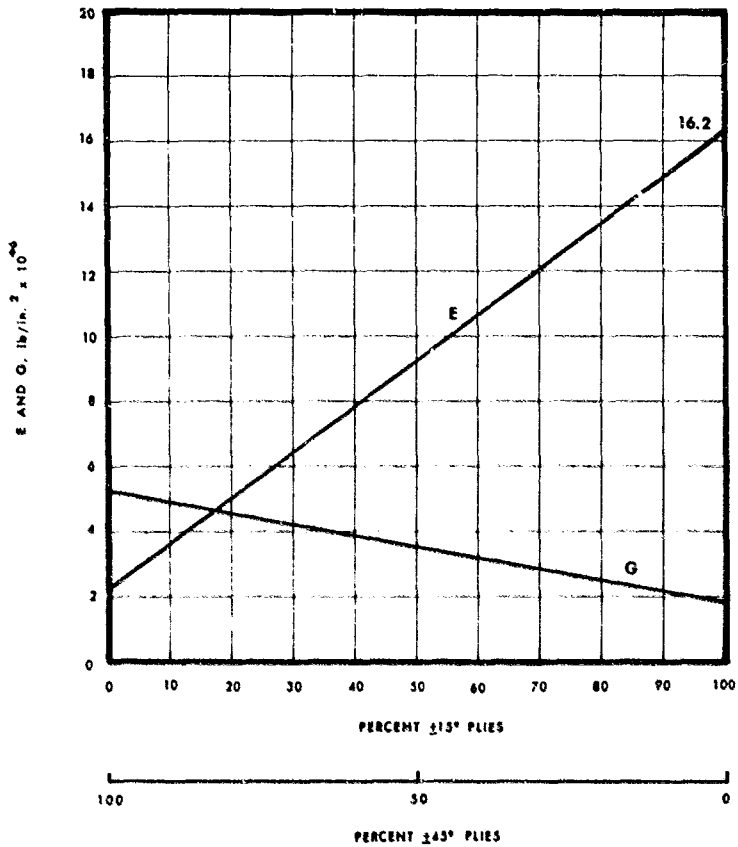


FIGURE 10. TENSILE AND SHEAR MODULUS FOR VARYING PERCENTAGES OF ±15° AND ±45° PLYS OF THORNEL 300.

FLAPWISE AND TORSIONAL STIFFNESS RATIO OF COMPOSITE SPAR TO DEMONSTRATOR SPAR,

$$\alpha_x = \frac{E I_{xx \text{ composite}}}{E I_{xx \text{ demonstrator}}} / \alpha_j = \frac{G J_{xx \text{ composite}}}{G J_{xx \text{ demonstrator}}}$$

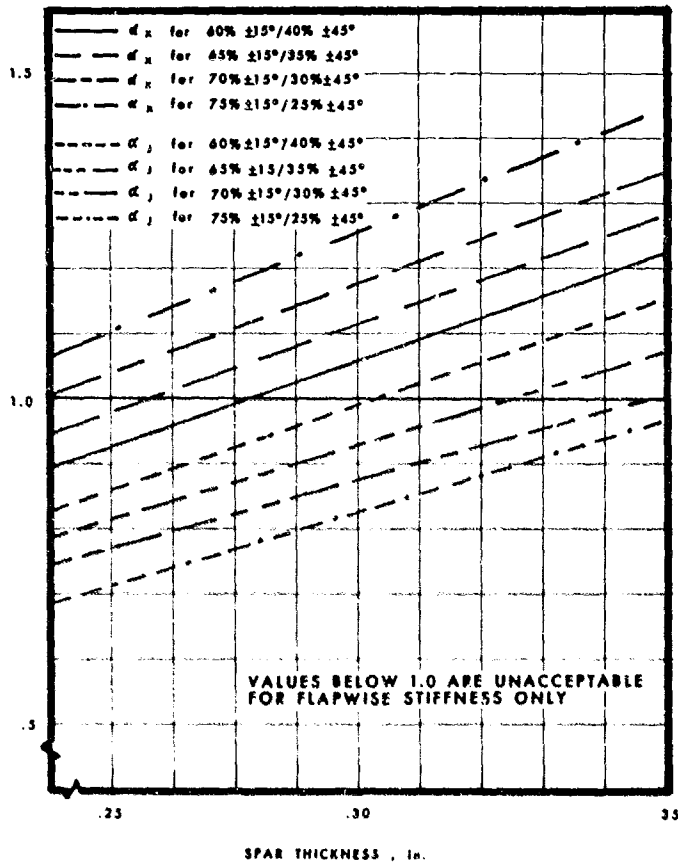


FIGURE 11. SPAR STATION 30 STIFFNESS RATIO vs SPAR THICKNESS FOR CONSTANT WINDING ANGLE.

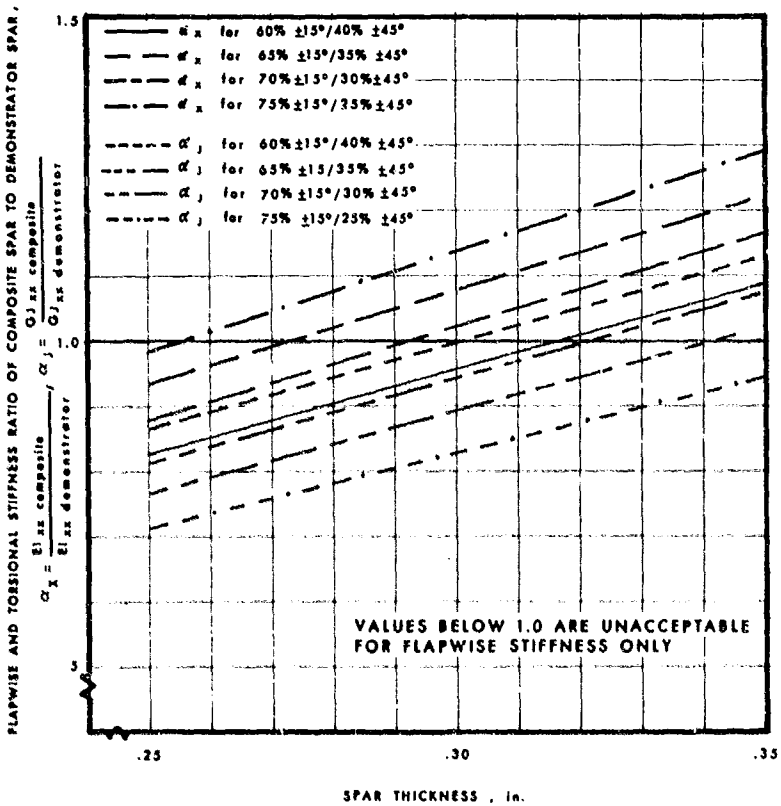


FIGURE 12. SPAR STATION 45 STIFFNESS RATIO vs SPAR THICKNESS FOR CONSTANT WINDING ANGLE.

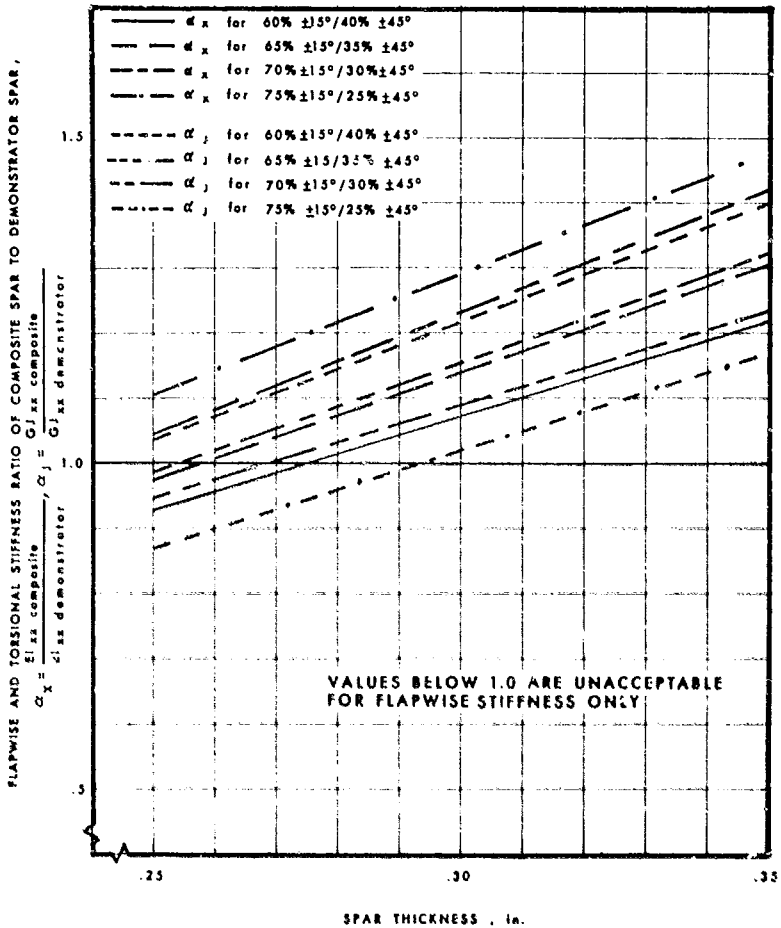


FIGURE 13. SPAR STATION 65 STIFFNESS RATIO vs SPAR THICKNESS FOR CONSTANT WINDING ANGLE.

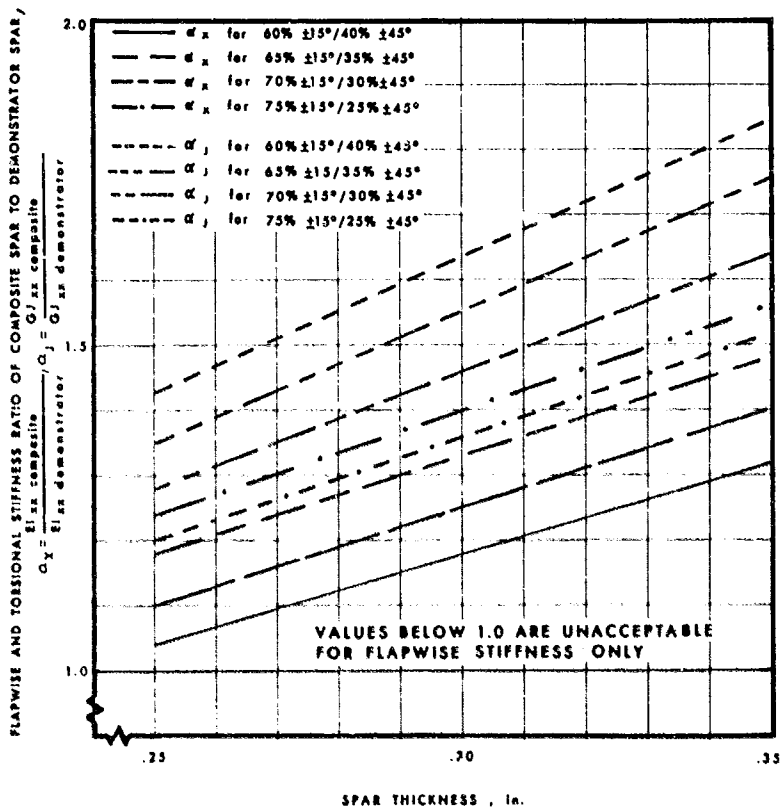


FIGURE 14. SPAR STATION 95 STIFFNESS RATIO vs. SPAR THICKNESS FOR CONSTANT WINDING ANGLE.

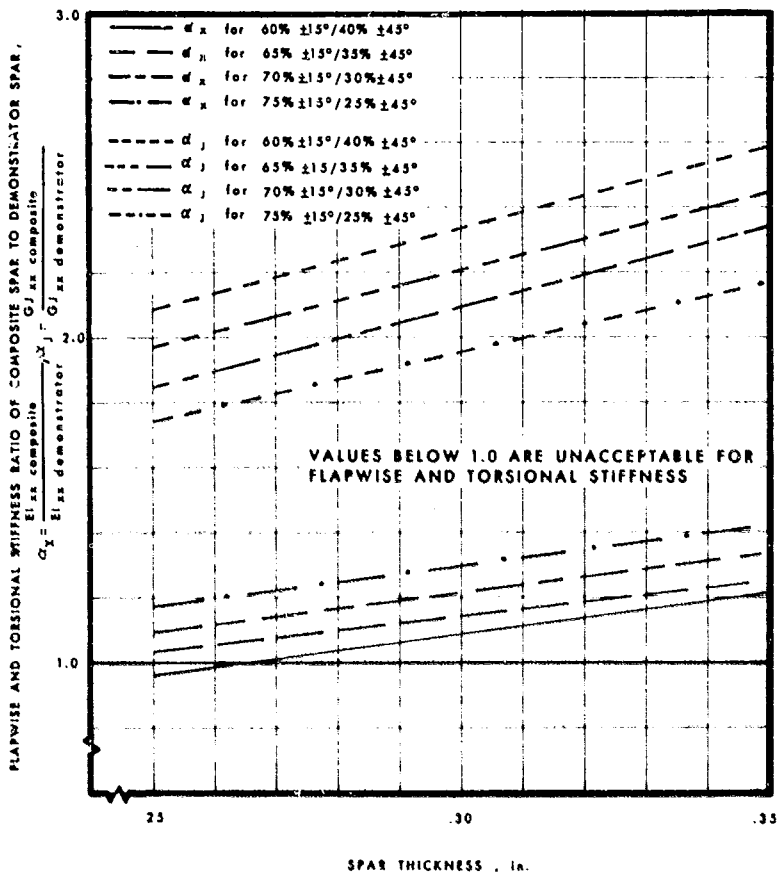


FIGURE 15. SPAR STATION 135 STIFFNESS RATIO vs SPAR THICKNESS FOR CONSTANT WINDING ANGLE.

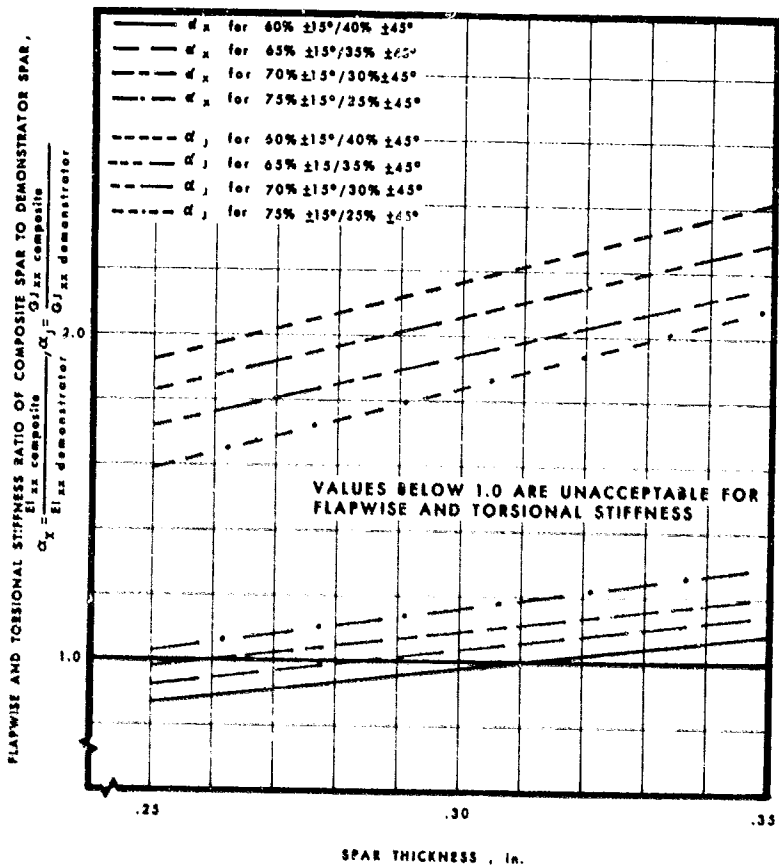


FIGURE 16. SPAR STATION 155 STIFFNESS RATIO vs SPAR THICKNESS FOR CONSTANT WINDING ANGLE.

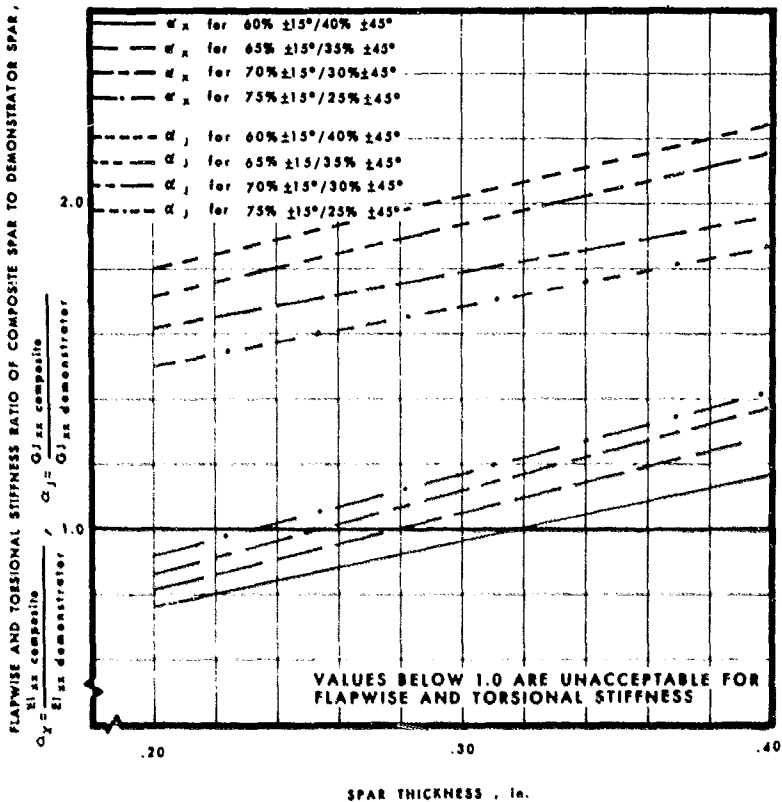


FIGURE 17. SPAR STATION 195 STIFFNESS RATIO vs SPAR THICKNESS FOR CONSTANT WINDING ANGLE.

Increasing the percentage of  $\pm 15^\circ$  plies in the laminate results in a thinner and lighter spar for the same flapwise stiffness. However, the requirement to closely match flapwise frequency with the demonstrator results in a limit in the percentage of these plies because of the superior stiffness to weight characteristics of the  $\pm 15^\circ$  composite lay-up relative to titanium. After careful study it was decided that the 70%  $\pm 15^\circ$ , 30%  $\pm 45^\circ$  combination would produce an attractive combination of spar weights, strain allowable and flapwise response characteristics.

With the proposed filament winding process, predetermined thickness requirements cannot be readily achieved. The process involves a constant carriage speed and constant rotational speed of the mandrel. Thus the variable diameter of the spar tube will result in a spanwise varying thickness for any one pass of the carriage. Thus to approximate the required theoretical thickness distribution some of the plies must be terminated along the blade span. The final thickness is also governed by the per-ply thickness of each roving. An achievable thickness distribution which approximates the theoretical value was determined as follows:

$$\text{Thickness/Ply} = \frac{\text{Area/Roving}}{(\text{Roving Band Width}) \times (\text{Fiber Volume Ratio})} \quad (3)$$

$$\begin{aligned} \text{where Area/Roving} &= 168.01 \times 10^{-6} \text{ in.}^2 \\ \text{Roving Band Width} &= .040 \text{ in.} \\ \text{Fiber Volume Ratio} &= .60 \end{aligned}$$

Therefore,

$$\text{Thickness/Ply} = \frac{168.01 \times 10^{-6} \text{ in.}^2}{(.040 \text{ in.}) \times (.60)} = .0070 \text{ in.} \quad (4)$$

Since there are two plies per layer (one plus and one minus), the thickness of a layer at the root end becomes

$$\text{thickness/layer} = .0140 \text{ in.}$$

For a constant winding angle, the relationship between the thickness/layer ( $t_n$ ) and the tube diameter at any particular point along the span of the spar is

$$t_n = .0140 \left( \frac{9.30}{\text{Diameter}} \right) \quad (5)$$

At various stations along the span of the spar, the thickness/layer is calculated and shown in Table 1.

TABLE 1. THICKNESS PER LAYER AS  
GOVERNED BY TUBE DIAMETER

Station	Tube Diameter (in.)	Thickness/Layer ( $t_n$ in.)
15	9.30	.01400
30	8.78	.01485
45	8.25	.01579
65	7.55	.01725
95	6.50	.0205
135	5.10	.0255
155	4.40	.0296
195	3.95	.0330

The actual total thickness which can be attained at each station is a function of the number of plies at that station.

$$N_{15} = (t_{req}) \times (\% \pm 15^{\circ} \text{ plies}) / t_n \quad (6)$$

$$N_{15} = t_{15}/t_n$$

$$N_{45} = (t_{req}) \times (\% \pm 45^{\circ} \text{ plies}) / t_n \quad (7)$$

$$N_{45} = t_{45}/t_n$$

Since  $N_{15}$  and  $N_{45}$  must be integer values, the values obtained from equations (6) and (7) are rounded off to the nearest integer value. The actual thickness of the spar at each station is now determined to be

$$t_{act} = (N_{15} + N_{45}) \times t_n \quad (8)$$

The actual spar thickness and number of plies for each station are shown in Table 2.

TABLE 2. ACHIEVABLE SPAR THICKNESS

Station	Theoretical Thickness Required			Number of Layers		Actual Thickness Achievable		
	t <sub>req</sub> (in.)	t <sub>15</sub> (in.)	t <sub>45</sub> (in.)	N <sub>15</sub>	N <sub>45</sub>	t <sub>15</sub> (in.)	t <sub>45</sub> (in.)	T <sub>act</sub> (in.)
15	.30	.210	.090	15	7	.210	.098	.308
30	.29	.203	.087	14	6	.208	.089	.297
45	.28	.196	.084	12	5	.1895	.079	.2685
65	.28	.196	.084	11	5	.1895	.0864	.2759
95	.28	.196	.084	10	4	.205	.0821	.2871
135	.27	.189	.081	7	3	.1785	.0765	.2550
155	.27	.189	.081	6	3	.1775	.0889	.2664
195	.26	.182	.078	6	2	.198	.066	.2640

ALTERNATE WINDING INVESTIGATION

To eliminate the fiber terminations along the blade spar, an alternative approach was investigated involving a variable carriage speed allowing the winding angle to vary along the span of the spar such that a constant thickness spar results. The angle of the plies at various spar stations as a function of the round tube diameter at that station is given by

$$\theta \text{ Station} = \frac{D \text{ Station}}{D \text{ Root}} \theta \text{ Root} \quad (9)$$

Requiring the ply orientations at the root end of the spar to be the same as for the previous approach involving a constant winding angle (i.e.,  $\pm 15^\circ$  and  $\pm 45^\circ$ ), the angle of each ply and the corresponding E and G values along the blade span are shown in Table 3.

TABLE 3. VARIATION OF E AND G FOR VARIABLE WINDING ANGLE AND CONSTANT THICKNESS

Spar Station	$\theta = \pm 15\%$ at Root			$\theta = \pm 45\%$ at Root		
	$\theta$	E	G	$\theta$	E	G
15	15.00	16.25	1.75	45.00	2.25	5.25
30	14.16	16.70	1.65	42.48	2.65	5.21
45	13.31	17.25	1.55	39.92	3.10	5.13
65	12.18	17.75	1.40	36.53	3.90	4.90
95	10.48	18.6	1.20	31.45	5.60	4.35
135	8.22	19.40	1.00	24.68	9.50	3.25
155	7.10	19.80	.90	29.29	12.0	2.85
195	6.37	20.0	.850	19.11	13.50	2.40

Using these values of E and G, along with the spar section properties from CRT for various spar thicknesses, the parameters  $\alpha_x$  and  $\alpha_y$  were again calculated for several spar stations. These parameters are plotted in Figures 18 through 24.

Since this type of winding results in a spar of constant thickness, it can be seen from Figures 18 through 24 that although the flapwise stiffness of the composite spar can be met at each station, the torsional stiffness cannot be matched at station 195 for a spar thickness less than .35 inch. Increasing the percentage of  $\pm 45^\circ$  plies at the root end will increase the torsional stiffness and decrease the flapwise stiffness along the span of the spar. Although this will reduce the thickness required to meet the torsional stiffness at station 195, it will not permit an accurate matching of flapwise stiffness. Therefore, the variable winding angle approach was not considered feasible for the ABC<sup>TM</sup> composite blade where it was required that flapwise stiffness be closely matched.

#### ROTOR BLADE PHYSICAL PROPERTIES

Physical properties of the composite spar sections were calculated using the spar thickness distribution shown in Table 2. These spar properties were substituted for those of the titanium spar in the section properties of the demonstrator blade. Properties through the root end attachment area were calculated based on structural sizing of this area from analysis shown further on in this report. The spanwise plots of the resulting composite blade physical properties are shown in Figures 25 through 29. Superimposed on these distributions are the corresponding distributions for the demonstrator blade.

It can be seen that the flapwise stiffness of the composite spar blade is approximately the same as that on the demonstrator blade except inboard where

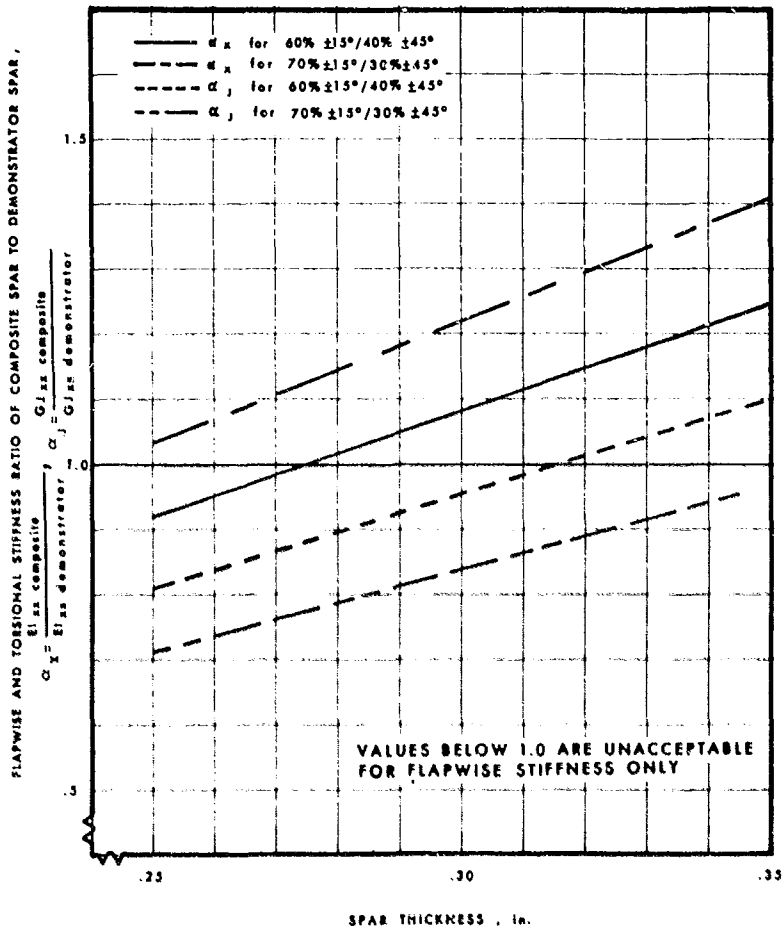


FIGURE 18. SPAR STATION 30 STIFFNESS RATIO vs SPAR THICKNESS FOR VARIABLE WINDING ANGLE.

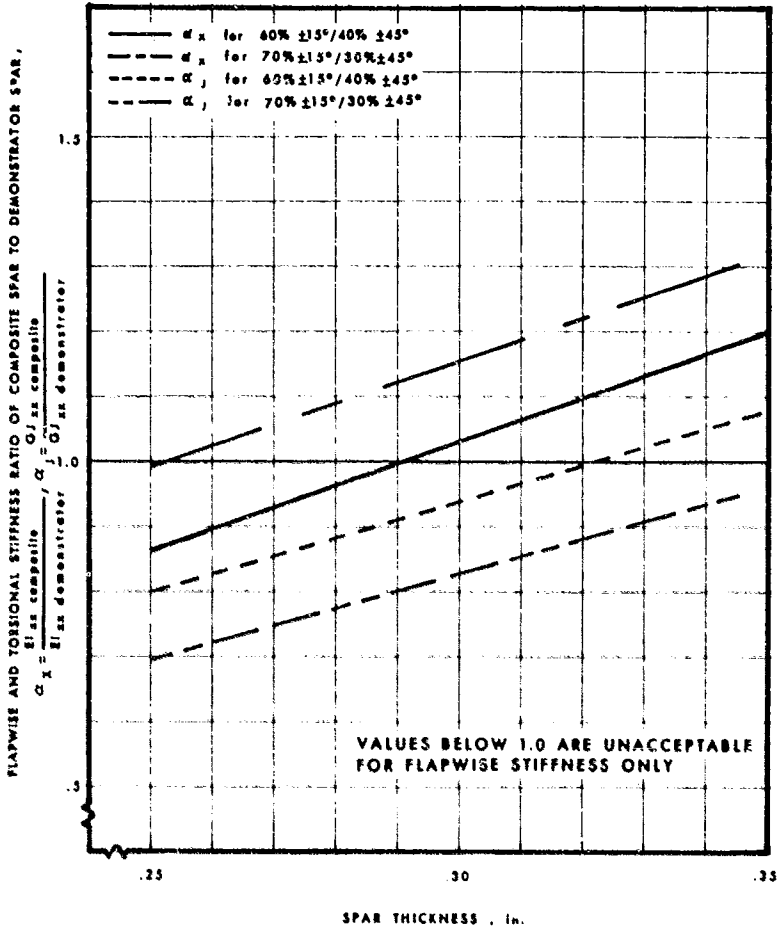


FIGURE 19. SPAR STATION 45 STIFFNESS RATIO vs SPAR THICKNESS FOR VARIABLE WINDING ANGLE.

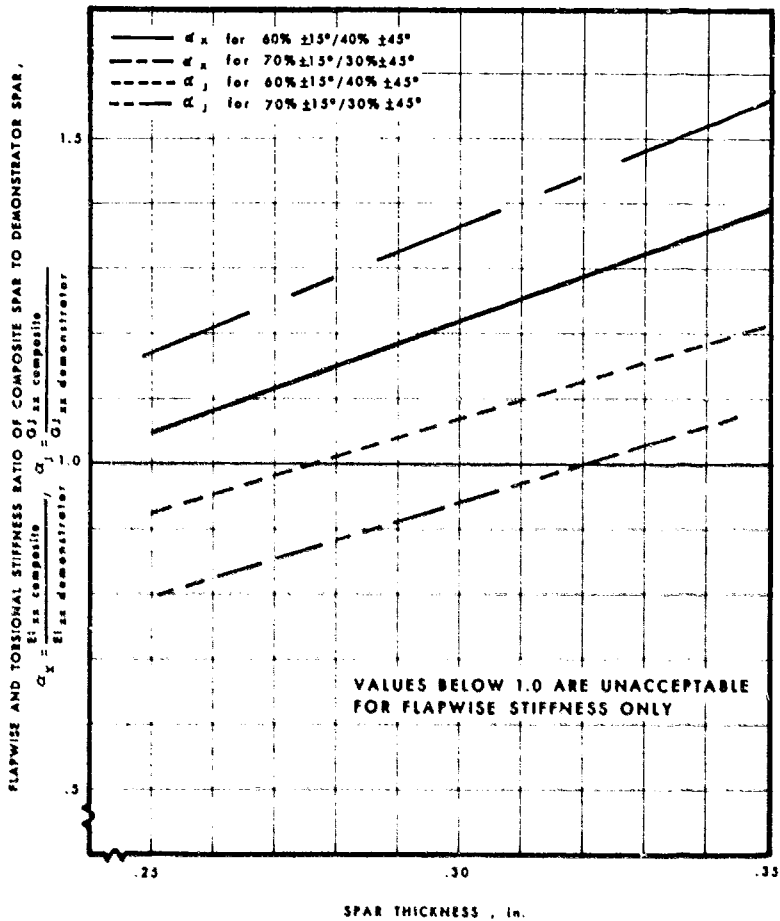


FIGURE 20. SPAR STATION 65 STIFFNESS RATIO vs SPAR THICKNESS FOR VARIABLE WINDING ANGLE.

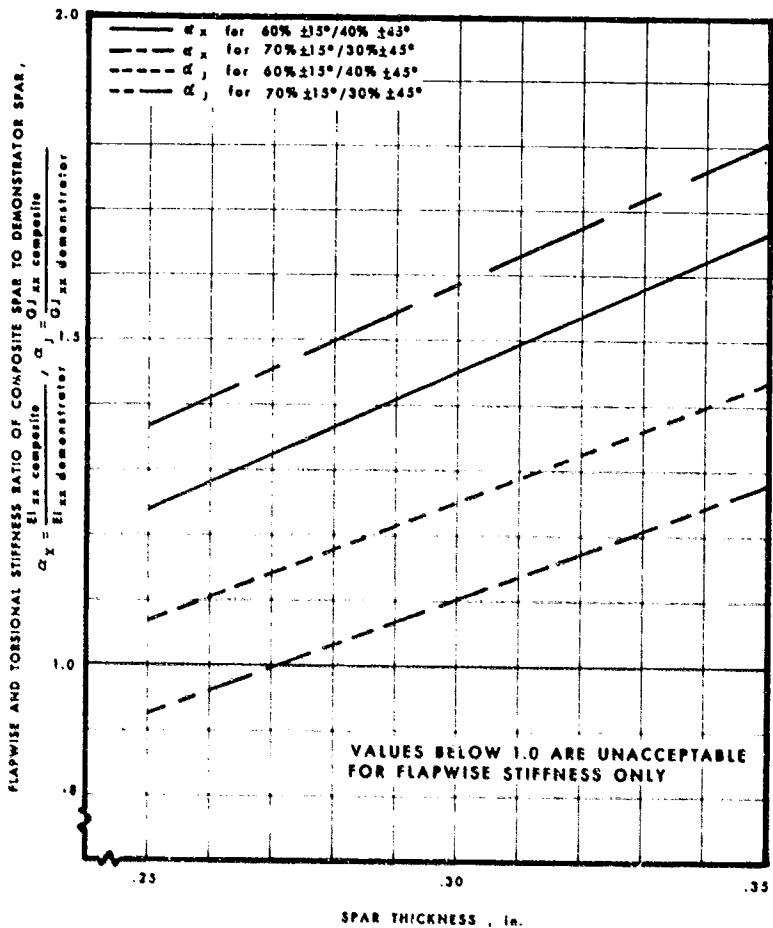


FIGURE 21. SPAR STATION 95 STIFFNESS RATIO vs SPAR THICKNESS FOR VARIABLE WINDING ANGLE.

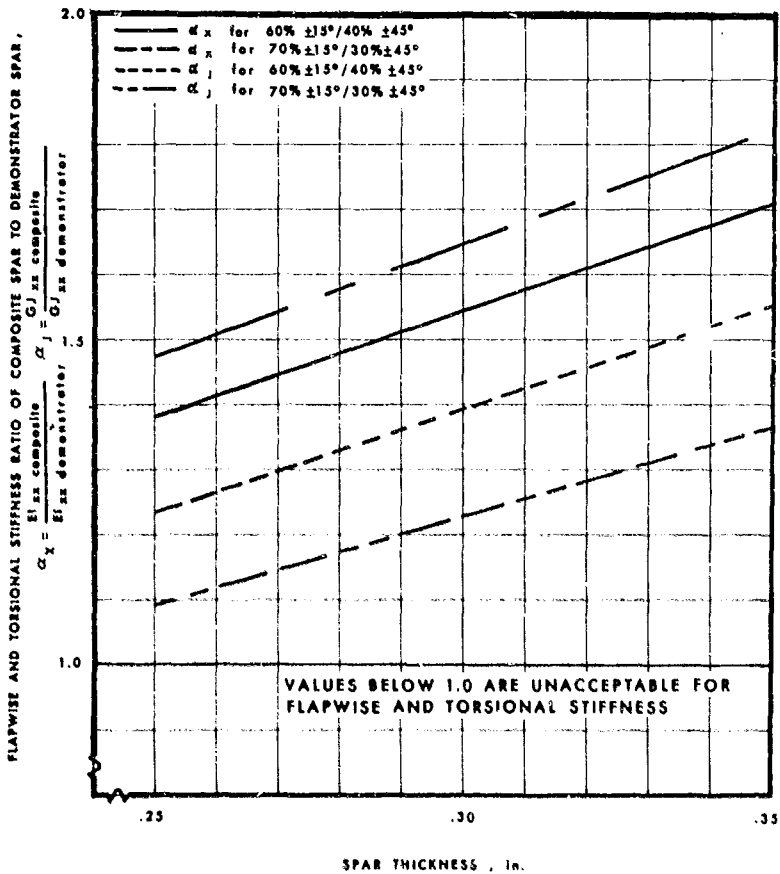


FIGURE 22. SPAR STATION 135 STIFFNESS RATIO vs SPAR THICKNESS FOR VARIABLE WINDING ANGLE.

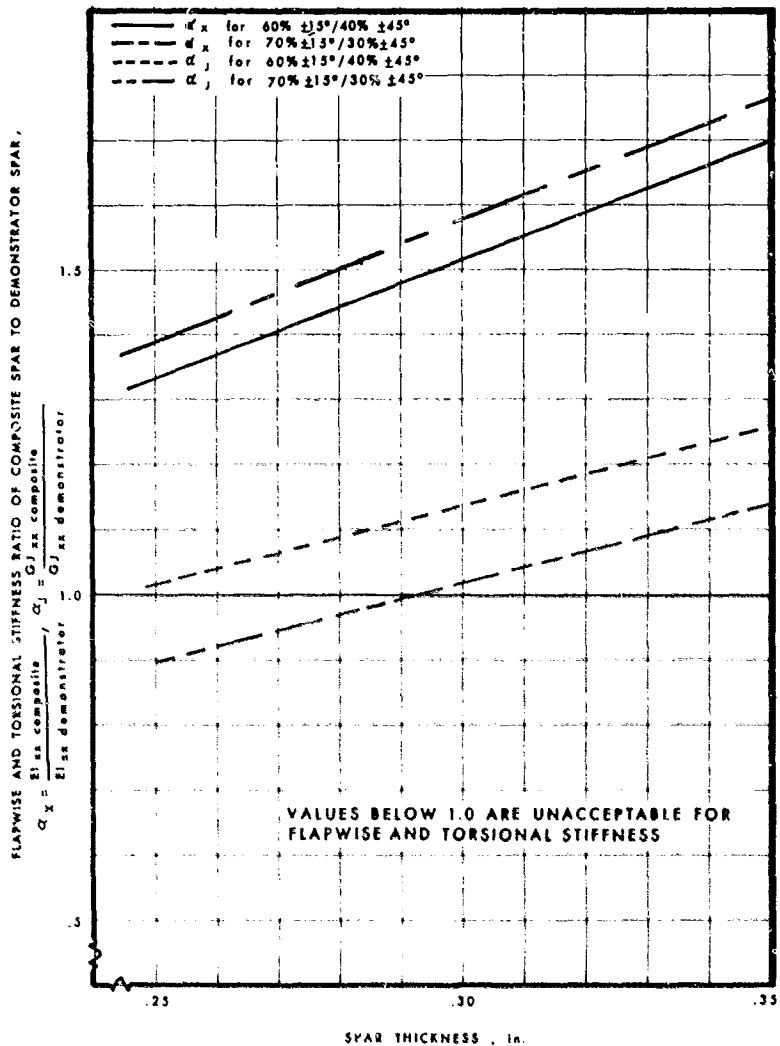


FIGURE 23. SPAR STATION 155 STIFFNESS RATIO vs SPAR THICKNESS FOR VARIABLE WINDING ANGLE.

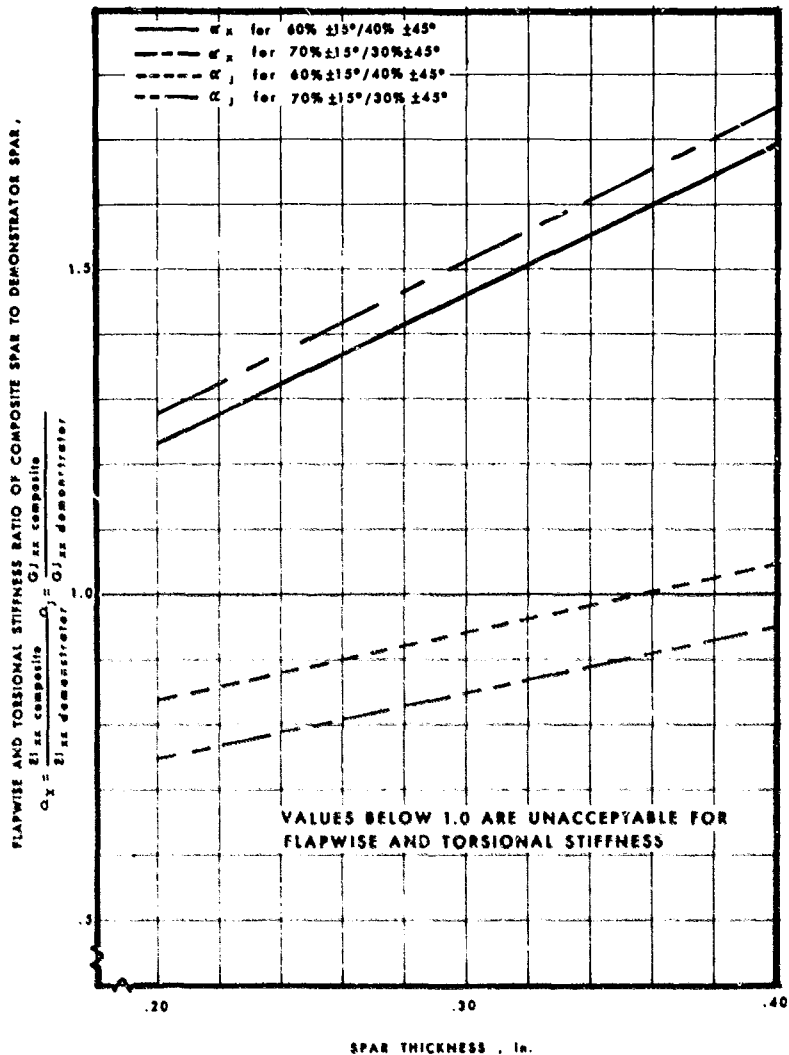


FIGURE 24. SPAR STATION 195 STIFFNESS RATIO vs SPAR THICKNESS FOR VARIABLE WINDING ANGLE.

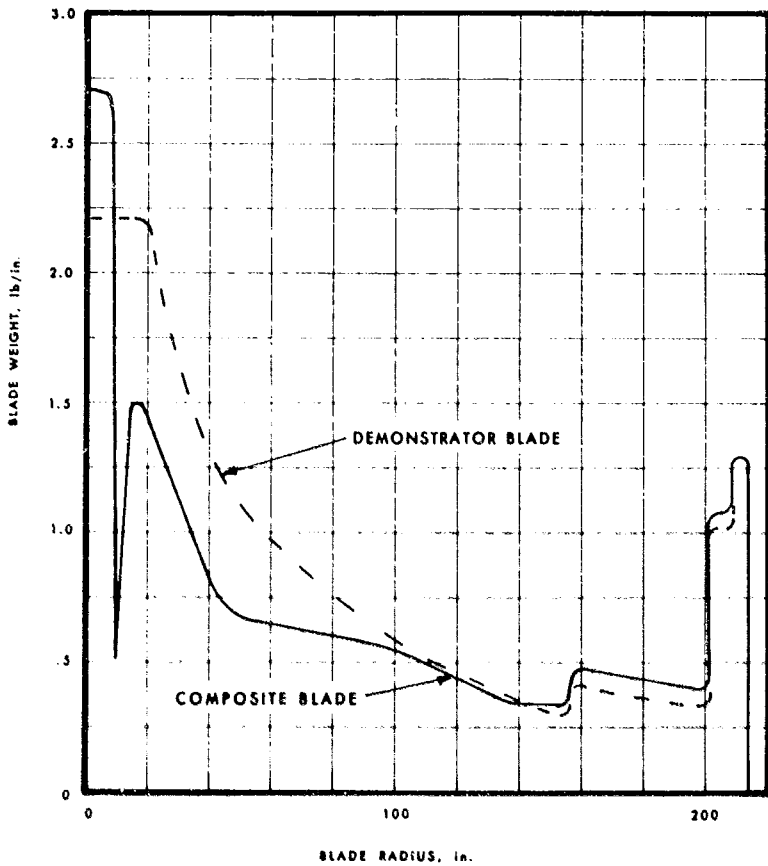


FIGURE 25. BLADE WEIGHT COMPARISON.

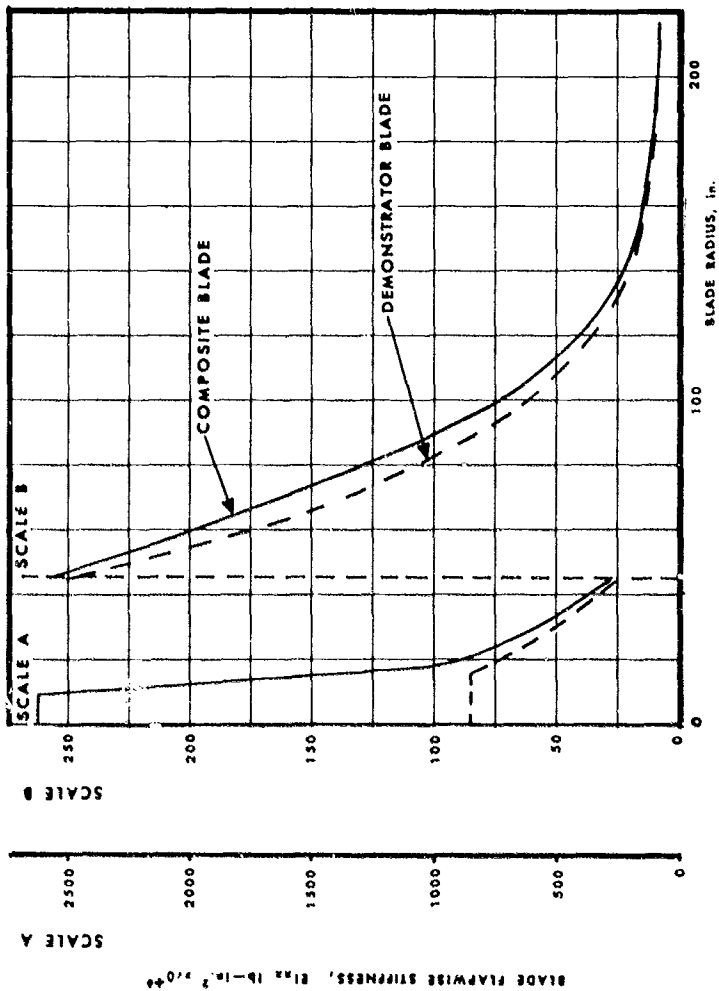


FIGURE 26. BLADE FLAPWISE STIFFNESS COMPARISON OF DEMONSTRATOR AND COMPOSITE BLADES.

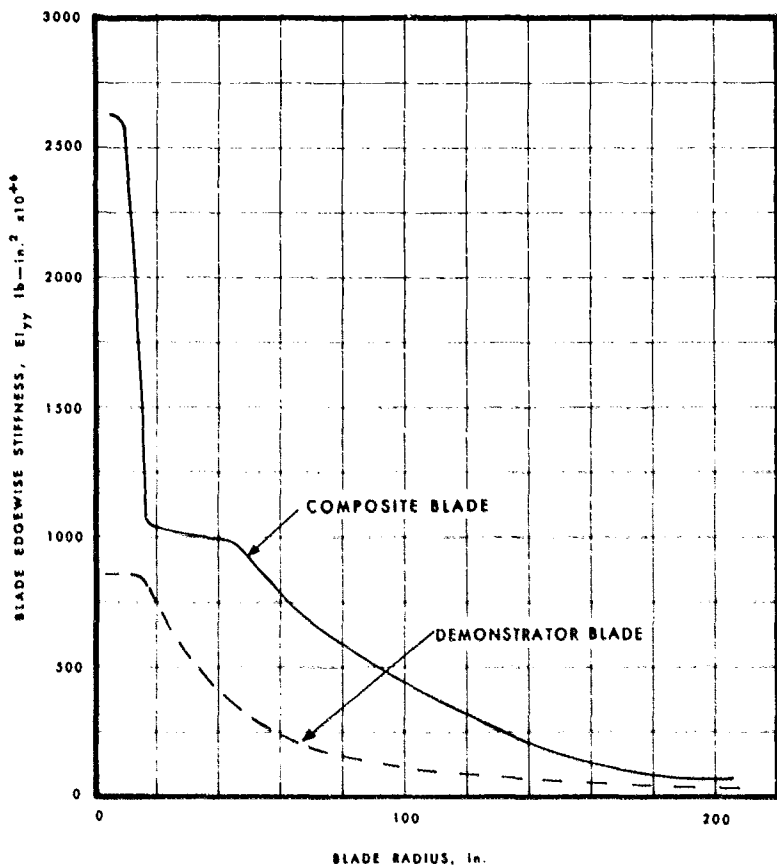


FIGURE 27. BLADE EDGEWISE STIFFNESS COMPARISON OF DEMONSTRATOR AND COMPOSITE BLADES.

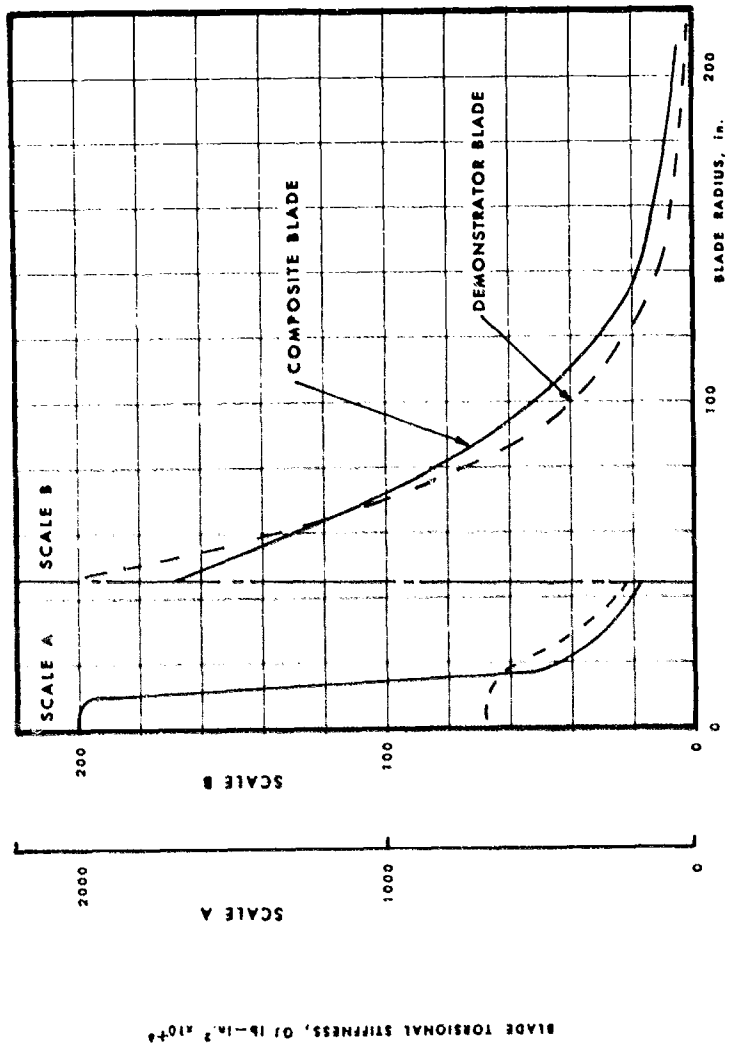


FIGURE 28. BLADE TORSIONAL STIFFNESS COMPARISON OF DEMONSTRATOR AND COMPOSITE BLADES.

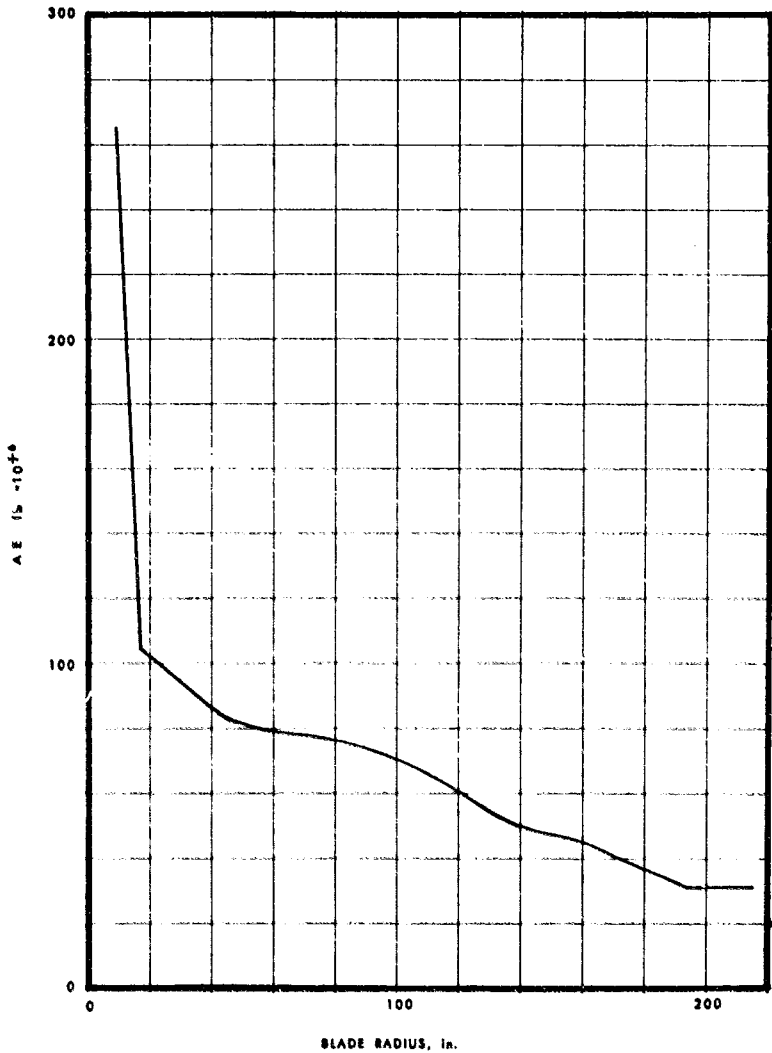


FIGURE 29. COMPOSITE BLADE AXIAL STIFFNESS.

the increased stiffness of the improved rotor hub is reflected. The blade weight distribution shows that the composite spar blade is significantly lighter than the demonstrator inboard of 50 percent radius except in the area of the hub. This demonstrates the superior stiffness to weight properties of the graphite epoxy material, resulting in a weight savings of 33 pounds with the filament winding approach. The weight savings occurs primarily in the inboard sections because the flapwise bending stiffness of these thicker airfoil sections was not seriously affected by the wall thickness required to match the stiffness of the titanium blade.

The chordwise stiffness of the composite blade is well above the demonstrator as was expected. Torsional stiffness is also above the titanium blade, especially in the more critical tip area.

#### DYNAMIC CHARACTERISTICS

The natural frequency spectrums of the demonstrator and composite blade are shown in Figures 30 and 31, respectively. Some important modal characteristics for the normal operating rpm are tabulated in Table 4. The following comparisons are noted below.

The frequencies of the first flapwise modes are almost identical which was a major goal of the design effort. Though the stiffness to weight ratio of the chosen composite lay-up exceeds that of titanium, and the flapwise stiffnesses of the two blades are similar, the matching of frequencies was still possible. This is because the weight savings were realized primarily in the inboard sections because the bending stiffness of these thicker airfoil sections was not seriously affected by the high wall thickness required to match stiffness. Thus the mass changes operate on those sections of the blade where the deflection in this mode is small, resulting in the small change in frequency.

The phase angle  $\theta$  represents the azimuth change between a one-per-rev force input and the maximum response of the mode to this input. This is important since this mode is the primary contributor to the control of the rotor through the one-per-rev control input. It is important that the phase angles between the rotor are similar if no changes are to be made to the control system. The phase angle of  $26.6^\circ$  for the composite blade compares favorably with the  $29^\circ$  value of the demonstrator blade. The reduction in damping of the mode is seen to have a small change in the damped modal amplification factors  $\mu_1$ , 1 and  $\mu_1$ , 2.

The placement of the higher flapping modes with respect to integer multiples of rotor speed is favorable as compared to the prototype.

The first edgewise mode frequency of the prototype was placed close to one-per-rev to provide separation from the first flapwise mode. The composite blade edgewise mode frequency is located closer to two-per-rev, providing approximately the same separation as in the demonstrator. The undamped modal amplification factor is seen to decrease due to one-per-rev excitation and increase appreciably due to two-per-rev excitation. Since the one-per-rev excitation is normally predominant, it was suspected that vibratory moments will not change appreciably in normal helicopter flight conditions.

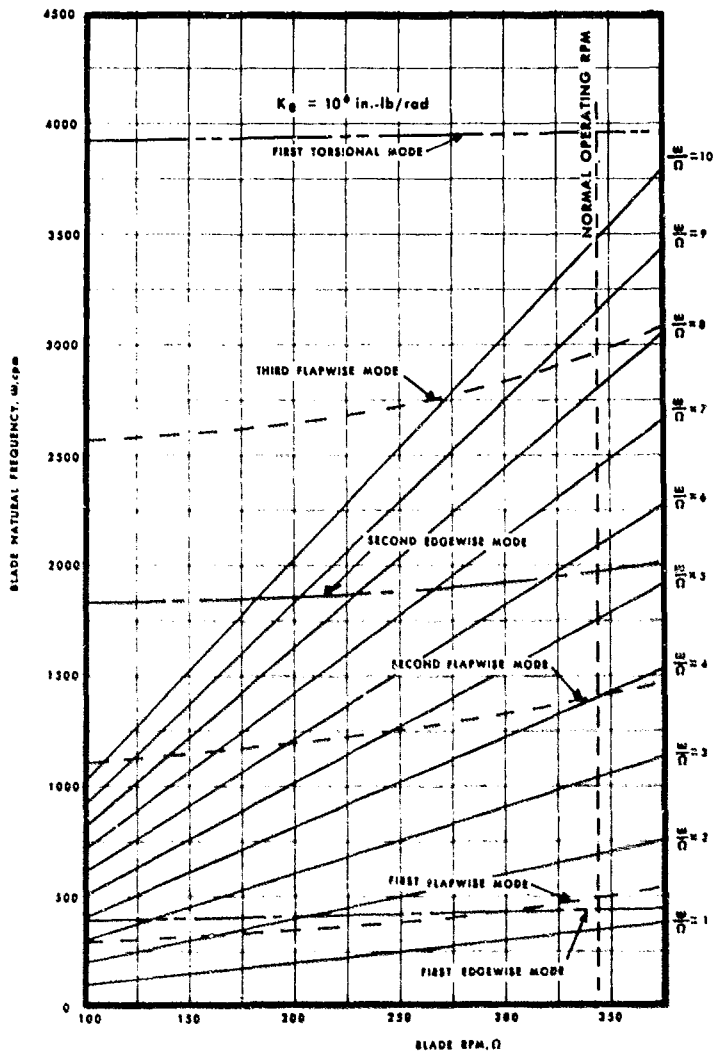


FIGURE 30. DEMONSTRATOR BLADE NATURAL FREQUENCY.

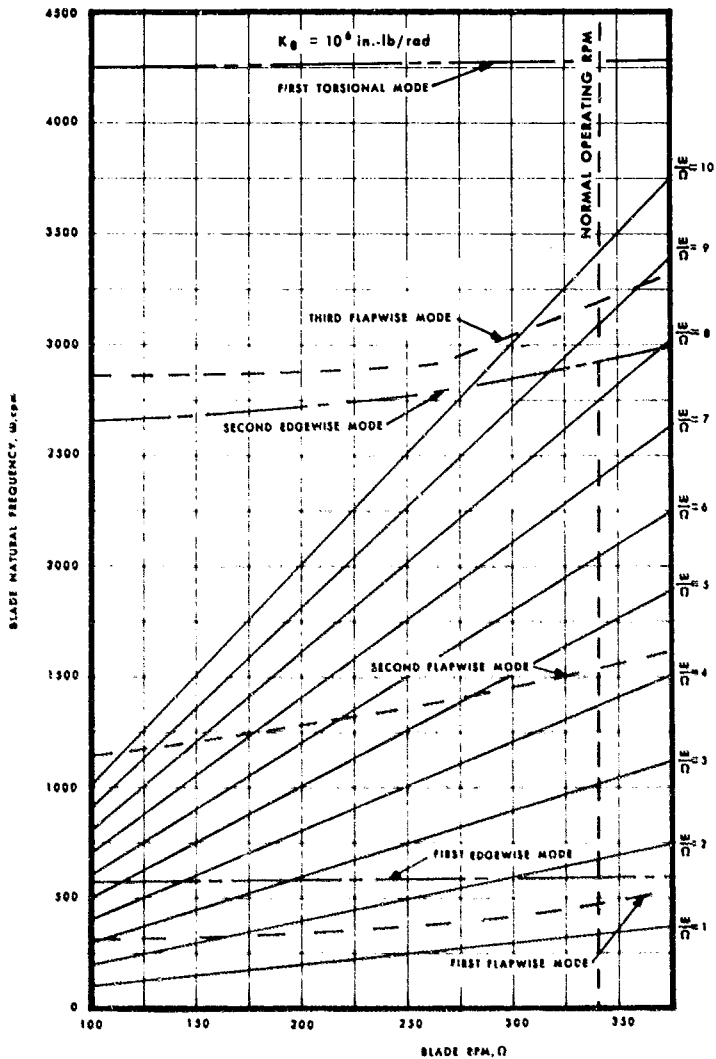


FIGURE 31. COMPOSITE BLADE NATURAL FREQUENCY.

The second edgewise mode frequency is well above that of the demonstrator blade and out of the range of typically predominant excitation frequencies.

The first torsion mode frequency is also above that on the prototype, reflecting the higher shear modulus to density ratio of the graphite epoxy lay-up relative to titanium. The mode is sufficiently high that amplification to typical predominant excitations is not of concern.

TABLE 4. PROPERTIES OF THE VIBRATION MODES AT NORMAL ROTOR SPEEDS

Mode	Item	Titanium Spar Blade	Composite Spar Blade
1st Flap	$\omega/\Omega$	1.46	1.47
	$\xi$	.189	.170
	$\phi$	29.0	26.6
	$\mu_{1,1}$	1.70	1.71
	$\mu_{1,2}$	.97	1.03
2nd Flap	$\omega/\Omega$	4.22	4.49
	$\xi$	.060	.060
	$\mu_{2,4}$	6.59	4.33
	$\mu_{2,5}$	2.32	3.61
3rd Flap	$\omega/\Omega$	8.55	9.34
	$\xi$	.029	.027
1st Chord	$\omega/\Omega$	1.29	1.76
	$\mu_{1,1}$	2.49	1.48
	$\mu_{1,2}$	.72	3.47
2nd Chord	$\omega/\Omega$	5.65	8.52
1st Torsional	$\omega/\Omega$	11.3	12.45

## LOADS DEVELOPMENT

Fatigue loads were determined using theoretical root bending and torsion moments from the demonstrator rotor blade analysis and determining the spanwise distribution using the moment shapes of the lowest flapwise bending and edgewise bending and torsion modes.

A single conservative condition was chosen under which the blade would be designed for infinite life. The selected blade root end loads correspond to a condition from the flight spectrum which occurs only .19 percent of the time.

$$M_F = \pm 228,000 \text{ in.-lb}$$

$$M_E = \pm 114,000 \text{ in.-lb}$$

$$M_T = \pm 37,000 \text{ in.-lb}$$

The bending moment distributions are shown in Figure 32 and the torsional moments in Figure 33.

Static limit loads were calculated for the ground flapping condition, ground starting condition and centrifugal force at overspeed RPM. The ground flapping condition consists of a uniform limit 2.67g flapwise acceleration field applied to the nonrotating blade. Ground starting loads are based on a limit torque corresponding to twice the military rated torque of the engines applied to the rotor. This is in combination with the limit lg flapwise moment. The overspeed RPM loads are calculated at 125 percent of normal rotor speed. The limit static torsional load is obtained from root end theoretical limit moments from the demonstrator blade, expanded spanwise according to the shape of the moment distribution of the first torsional mode. Spanwise plots of the limit loads corresponding to these conditions are shown in Figures 34 through 36.

The ultimate loads are obtained by multiplying the limit values by 1.5.

## BLADE STRESS ANALYSIS

Combined bending and tension strains were calculated both at the spar aft corner radius and at the trailing edge. For fatigue cases the edgewise and flapwise moments were conservatively assumed to act in phase. Figure 37 shows the notation used in calculating strains.

Torsional shear strains were calculated only in the spar structure since the aft skin is less critical than in the demonstrator blade.

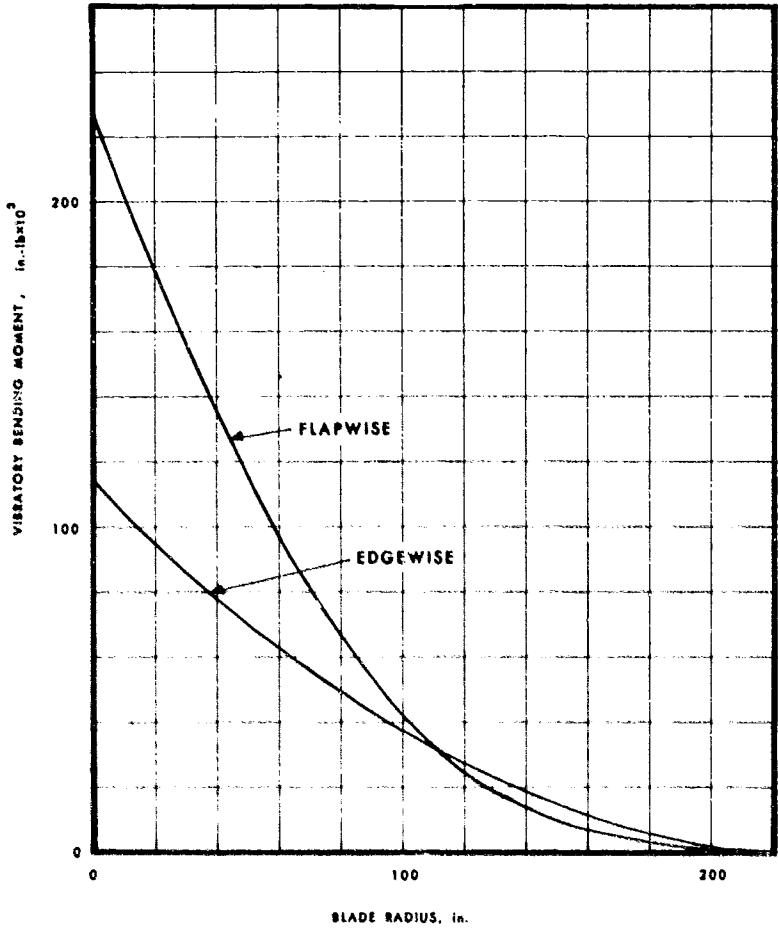


FIGURE 32. BLADE VIBRATORY BENDING MOMENTS.

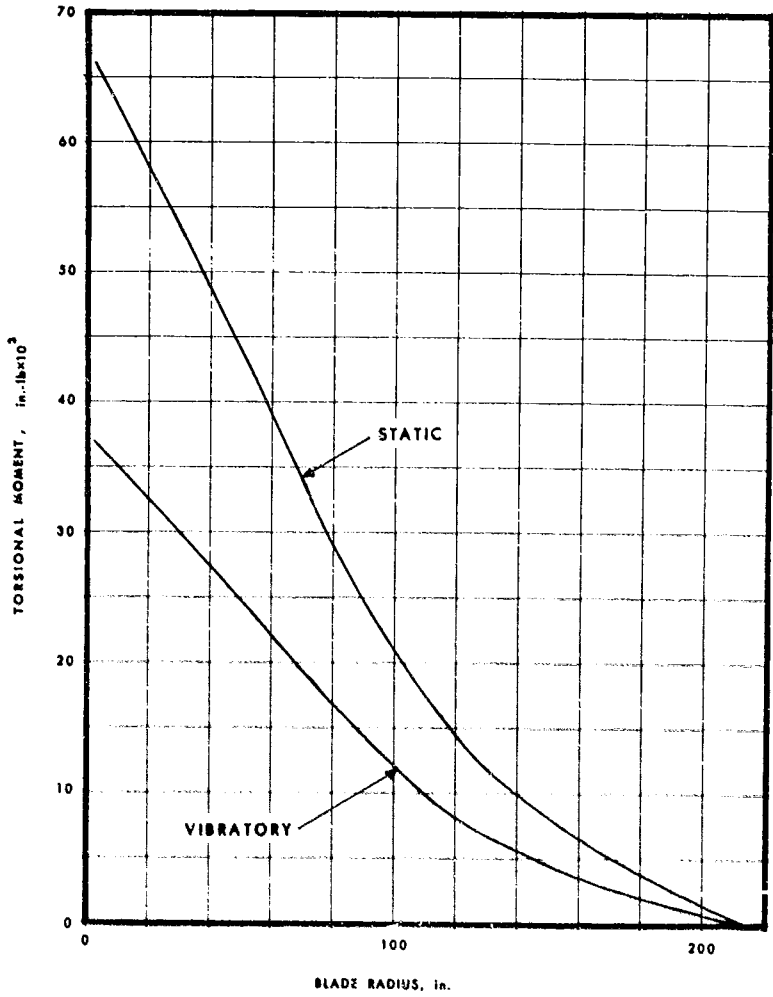


FIGURE 33. BLADE TORSIONAL MOMENT.

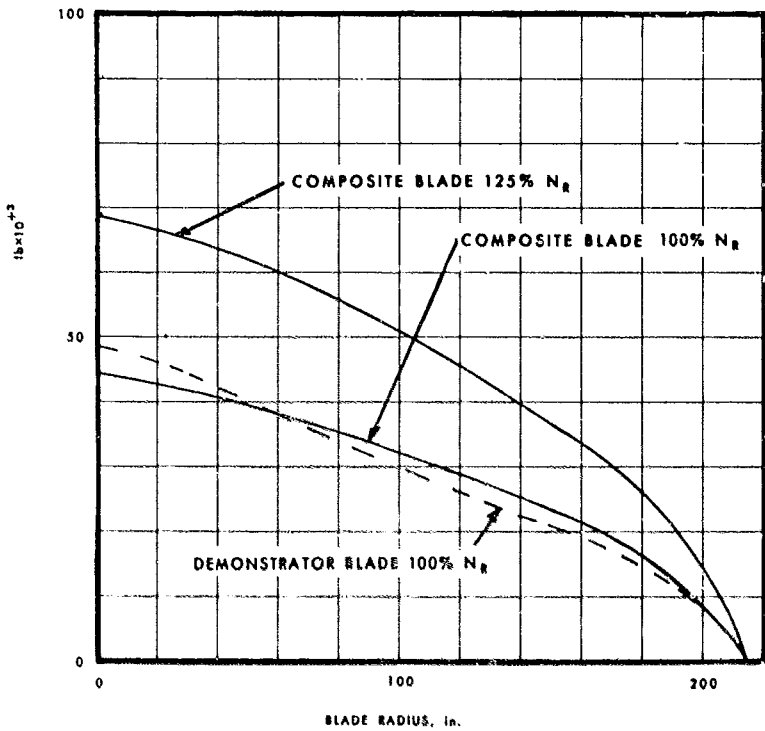


FIGURE 34. BLADE CENTRIFUGAL FORCE.

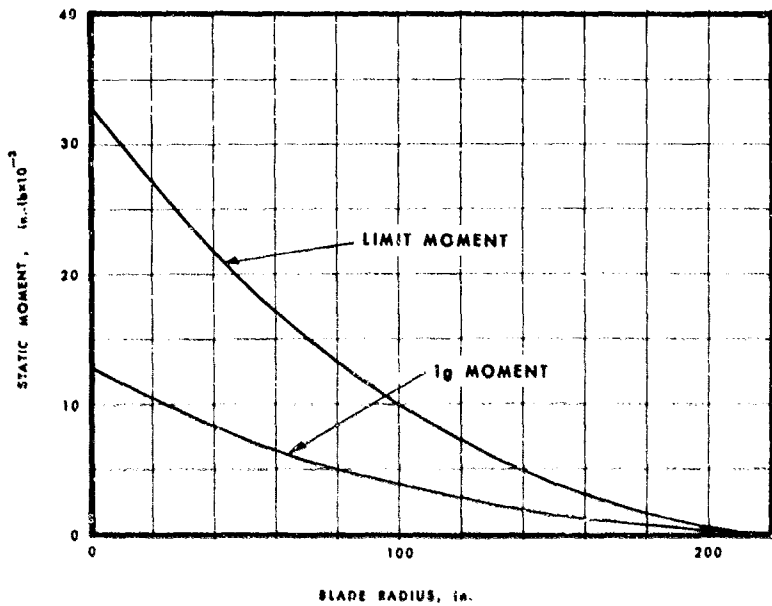


FIGURE 35. BLADE FLAPWISE STATIC MOMENT.

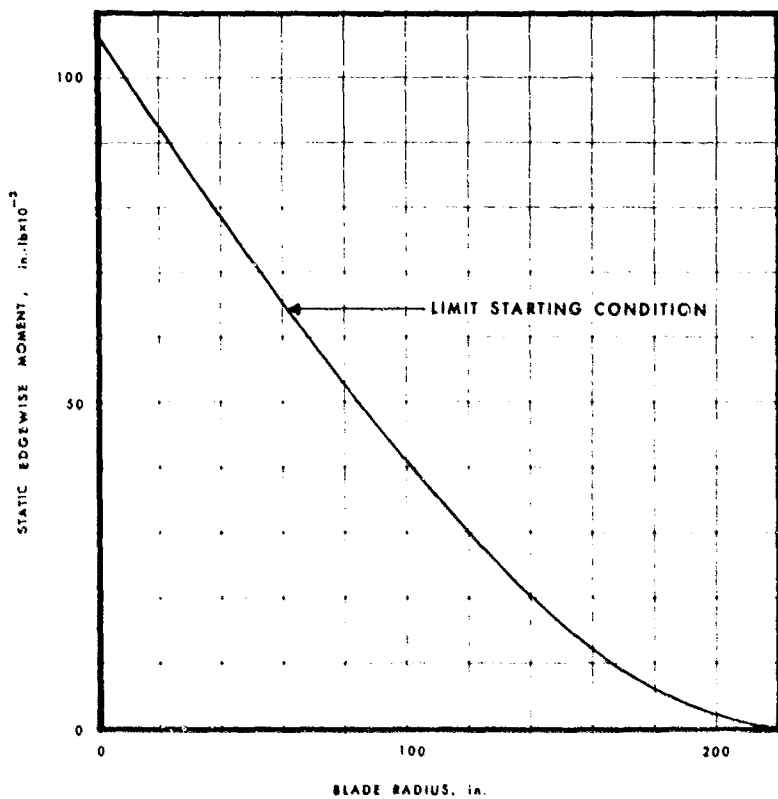


FIGURE 36. BLADE EDGEWISE STATIC MOMENT.

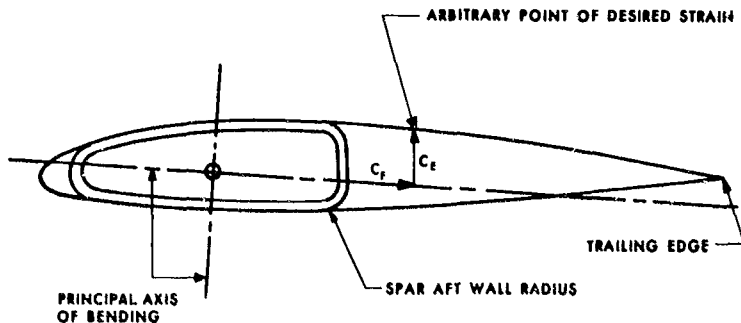


FIGURE 37. NOTATION USED FOR STRAIN CALCULATIONS.

The following equations were used to determine the fatigue strain levels and margins of safety. The results are shown in Tables 5 and 6.

$$\epsilon = \frac{M_F C_F}{E I_{xx}} + \frac{M_E C_E}{E I_{yy}} + \frac{C_F}{AE}$$

$$\gamma = \frac{M_T}{2A'Gt}$$

where

$$A' = \sqrt{\frac{J_u}{At}} = \text{Mean enclosed area of spar, in.}$$

$$MS = \frac{\epsilon_{\text{allow}}}{\epsilon} - 1.0 \text{ for axial strain}$$

$$MS = \frac{\gamma_{\text{yellow}}}{\gamma} - 1.0 \text{ for shear strain}$$

Fatigue allowables for Thornell 300 were derived from small specimen test data and similar modulus graphite.

TABLE 5. BLADE FATIGUE STRAIN SUMMARY

Blade Station	M <sub>F</sub> (in.-lb)	M <sub>G</sub> (in.-lb)	r (in.-in)	Spar Backwall Strain (µin./in.)	M.S.	Trailing Edge Strain (µin./in.)	M.S.	Spar Shear Strain (µin./in.)	M.S.
30	±146,000	±56,000	±30,000	±937	+ .387	±1230	+ .057	±344	+ High
45	±126,000	±75,000	±26,000	±1214	+ .071	±930	+ .383	±462	+ High
65	± 90,000	±60,000	±21,000	±1164	+ .117	±945	+ .376	±404	+ High
95	± 48,000	±40,000	±13,500	±964	+ .349	±800	+ .625	±430	+ High
135	± 16,000	±21,000	± 6,250	±717	+ .813	±727	+ .788	±417	+ High
155	± 8,000	±14,000	± 4,000	±430	+ High	±609	+1.135	±358	+ High
195	± 1,000	± 3,000	± 1,000	±120	+ High	±227	+ High	±127	+ High

TABLE 6. BLADE ULTIMATE STRAIN SUMMARY

BLADE STA.	F LIMIT (lb)	M <sub>F</sub> LIMIT (in.-lb)	M <sub>F</sub> LG (in.-lb)	M <sub>W</sub> LIMIT START (in.-lb)	ULT STRAIN ACROSS SECT.		ULT STRAIN BACKWALL		ULT STRAIN TRAILING EDGE		
					in. OVER SPEED COND.	in. / GROUND FLAME PING	in. / in.	in. / in.	in. / in.	STARTING CONDITION	
30	65000	24500	9000	86000	1015	+High	161	+High	505	1848	+High
45	65000	21000	7500	76000	1122	+High	238	+High	484	1432	+High
65	59000	16500	6000	63000	1111	+High	249	+High	500	1484	+High
95	51000	11000	4000	44000	1045	+High	262	+High	429	1314	+High
125	41000	5700	2000	23000	1186	+High	282	+High	382	1191	+High
155	35000	3000	1500	14000	1121	+High	220	+High	319	900	+High
195	20000	1000	500	2000	953	+High	101	+High	104	227	+High

These data indicated mean tension strain endurance limits of  $\pm 3700$   $\mu\text{in./in.}$  and  $\pm 2600$   $\mu\text{in./in.}$  for the  $\pm 15^\circ$  and  $\pm 45^\circ$  directions respectively at stress ratios of .10.

The rule of mixtures was used to determine the axial strain allowable of the composite lay-up used in the filament-wound spar design, i.e.,  $70\% \pm 15^\circ$  and  $30\% \pm 45^\circ$ .

$$\epsilon = .70 (\pm 3700 \mu\text{in./in.}) + .30 (\pm 2600 \mu\text{in./in.})$$

$$\epsilon = \pm 3300 \mu\text{in./in.}$$

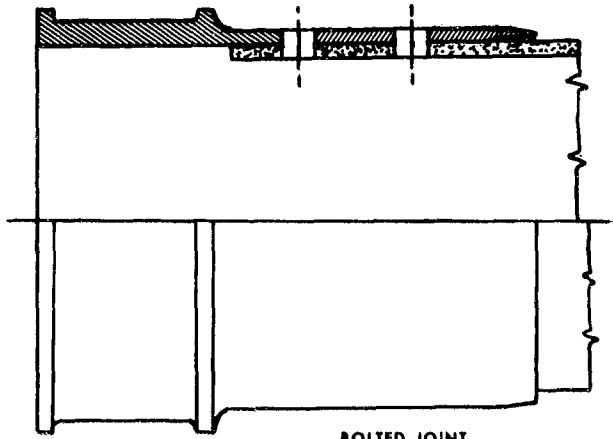
The working fatigue strain allowable was then established to be one-half the mean value. Since the fatigue data available was based on  $10^7$  cycles, it was conservatively assumed that at  $10^8$  cycles the mean value of strain would be 80% of the strain level at  $10^7$  cycles. This results in an axial working fatigue strain of  $\pm 1300$   $\mu\text{in./in.}$  A similar procedure was followed for the allowable shear strain. The resulting shear strain allowable was found to be  $\pm 2000$   $\mu\text{in./in.}$

#### ROOT END ATTACHMENT

In the final rotor blade assembly, the spar must transition into a titanium fitting which acts as the internal bearing support for the pitch bearings. Several configurations were considered to provide a structural interface between the composite filament-wound spar and the titanium root end.

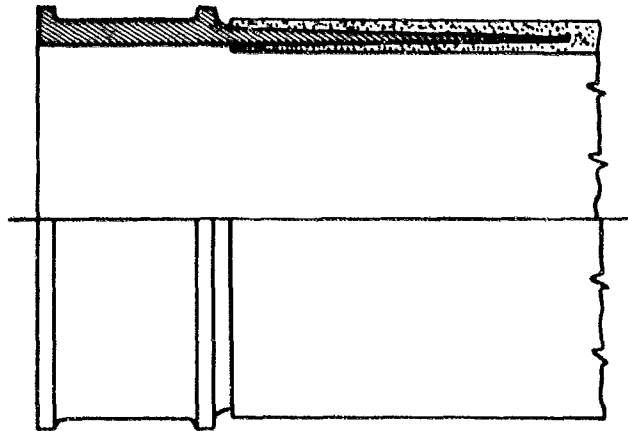
A bolted attachment between the composite and titanium was one alternative (Figure 38). This type of joint requires a composite thickness well in excess of the basic spar thickness in order to develop the required strength across the holes. The increased thickness would require additional hand lay-up operations after forming to achieve this buildup. An alternative approach was desired which was more compatible with the filament winding technique. A double bonded constant-diameter cylindrical fitting, as shown in Figure 39 was considered to be compatible with the filament winding operation in that the connection could be made during the winding operation. However, no alternative load path is present in the event of a bond failure.

An improvement over this configuration provides for a double-bonded tapered cylindrical fitting, shown in Figure 40. The taper provides a secondary load path which, in the event of a bond failure, is capable of reacting the load through purely mechanical wedging action. However, certain disadvantages were obvious. Kick loads produced at the beginning of the taper will produce tension components which tend to debond the inner portion of the graphite in the double bond configuration. The tendency of interlaminar splitting also exists under compression loadings in the double bond configuration. Also, inspection of the internal bond is difficult and the manufacturing is not an easy task.



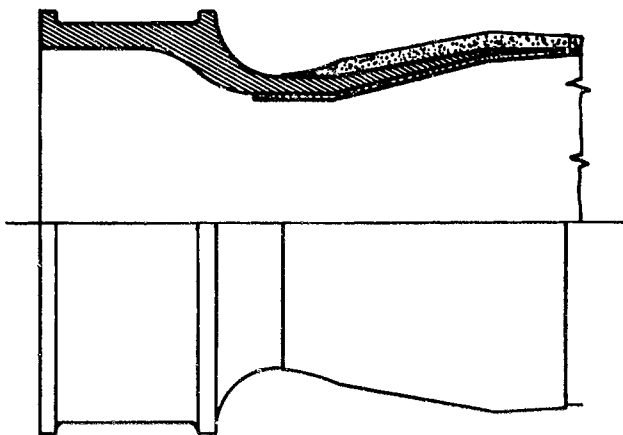
**BOLTED JOINT**

**FIGURE 38. ROOT END ATTACHMENT—BOLTED JOINT.**



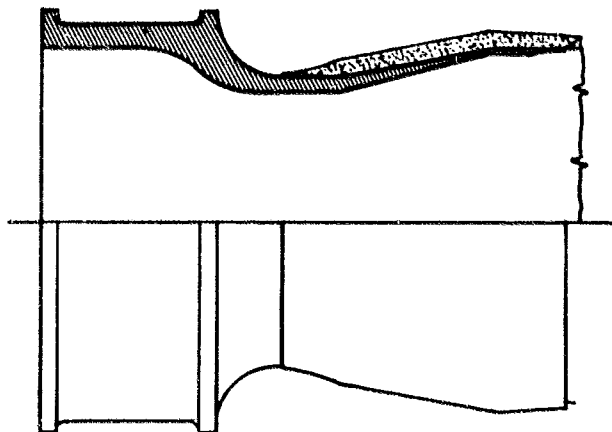
**BONDED JOINT**

**FIGURE 39. ROOT END ATTACHMENT—BONDED JOINT.**



DOUBLE-BONDED TAPERED CYLINDER

FIGURE 40. ROOT END ATTACHMENT— DOUBLE-BONDED TAPERED CYLINDER.



SINGLE-BONDED TAPERED CYLINDER

FIGURE 41. ROOT END ATTACHMENT— SINGLE-BONDED TAPERED CYLINDER.

A further improvement was made to this configuration by providing only a single bonded surface such that the titanium fitting is completely inside the composite structure (Figure 41). Though this provides less bond area between the composite and the titanium, the significant disadvantages of interlaminar splitting and the internal bonding risk were eliminated.

Thus the simple single-bond tapered cylindrical fitting was chosen as the most attractive root end attachment for the filament-wound spar.

#### ANALYSIS OF BOND JOINT

Shear stresses in bonded joints are most critical at the joint extremities where the predominant shear transfer occurs between the two bonded materials. To reduce the high shear stress peaks that tend to occur in these areas, it is necessary to tailor the local thickness distribution to minimize stiffness discontinuities of the joint extremities, thus providing a more gradual transfer of load.

Preliminary designing of the bond length and thickness distribution at the extremities of both the titanium and composite material was accomplished using the Sikorsky one-dimensional bond joint analysis. To obtain a model consistent with the assumptions of the program, a unit angular segment of the circumference was considered to carry a constant load over the whole bond length. The variation of the bond area and material thickness with the radius at the bond joint was considered in the analysis. Figure 42 illustrates this technique.

The applied loads to the segments were derived from the maximum vibratory combined bending stress in the spar just outboard of the fitting.

$$F_{\text{segment}} = \frac{\sigma}{\text{combined outboard}} \times \text{area outboard segment}$$

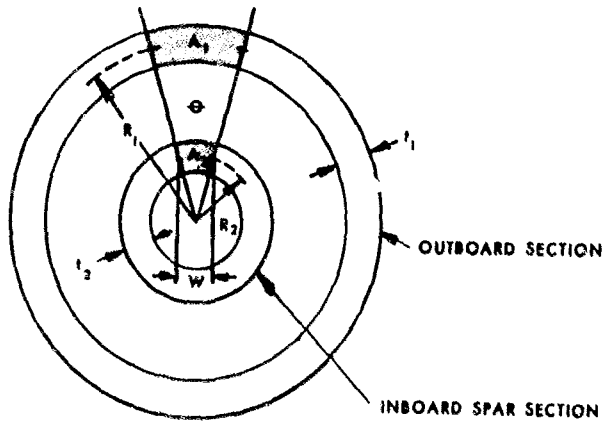
Only fatigue loads were used for the root end analysis since static loads were found to be less critical. In the design of the root end attachment it was desired to keep the peak vibratory bond shear stress below  $\pm 2000$  psi. This allowable was based upon correlation of fatigue test data on adhesive joints with the bond joint computer program analysis for peak bond shearing stress.

The thickness of the composite material was held constant over the full incline length at the value established to meet stiffness requirements just outboard of the fitting.

For this analysis thickness of the titanium at the root end of the joint was sized to carry the full fatigue bending loads based on an assumed diameter (Figure 43).

The fatigue allowables were established by using small specimen fatigue test data in the form of a "Constant Life Fatigue Diagram" (also known as a "Goodman Diagram"). Using the calculated value of steady stress, a mean S/N curve was established relating allowable vibratory stress and cycles to failure.

ANGULAR SEGMENT ANALYZED



$$A_1 = R_1 \odot t_1$$
$$A_2 = R_2 \odot t_2$$

FIGURE 42. SEGMENTS USED IN BOND JOINT ANALYSIS.

COMPOSITE MATERIAL



TITANIUM FITTING



FIGURE 43. MODELING OF STRUCTURE FOR BOND STRESS STUDY—ACTUAL STRUCTURE.

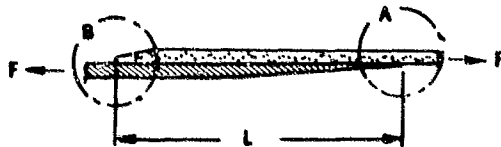


FIGURE 44. MODELING OF STRUCTURE FOR BOND STRESS STUDY—MODEL USED FOR ONE-DIMENSIONAL ANALYSIS.

A working allowable was generated for infinite life by reducing the mean endurance limit from this curve by factors accounting for size effects, stress concentration, surface finish and reliability. This was calculated by

$$\sigma_{v \text{ working}} = \frac{\sigma_{v \text{ mean}}}{K_f K_{fs}} (F_s) (F_r) \quad (20)$$

where  $\sigma_{v \text{ working}}$  = the working fatigue endurance limit

$\sigma_{v \text{ mean}}$  = the mean endurance limit established from the S/N diagram

$K_f$  = the reduction factor due to stress concentration factors

$K_{fs}$  = the reduction factor due to surface finish effects

Using equation (20) the vibratory stress endurance limit for B-STOA titanium with a stress concentration factor included is  $\pm 18,000$  psi. Working with an incline angle of  $10^\circ$  and assuming the length of the incline to be 4.0 inches, the outside diameter of the titanium fitting was established to be 7.3 inches at the base of the incline. Under the combined flapwise and edgewise bending moment of  $\pm 255,000$  in.-lb., the required moment of inertia (I) of the section was established to be

$$I = \frac{MR}{\sigma_{v \text{ ALL}}}$$

$$I = \frac{(\pm 255,000) (3.65)}{\pm 18,000}$$

$$I = 51.7 \text{ in.}^4$$

The required thickness was established to be

$$t = .40 \text{ inch}$$

Using the model shown in Figure 44, an iteration study was conducted where-in the taper geometry at A and B were varied and also the overall length, L, of the bonded joint.

The effect of varying the end taper in the titanium material at A and the composite material at B is shown in Figure 45. The aforementioned peaking of the bond stresses at the joint extremities is obvious. For the cases investigated, a parabolic taper in both the titanium and composite extremities produced the lowest peak shearing stresses. Other geometry modifications could obviously have produced an even more attractive stress distribution. However, this one proved to be structurally acceptable, as will be discussed later.

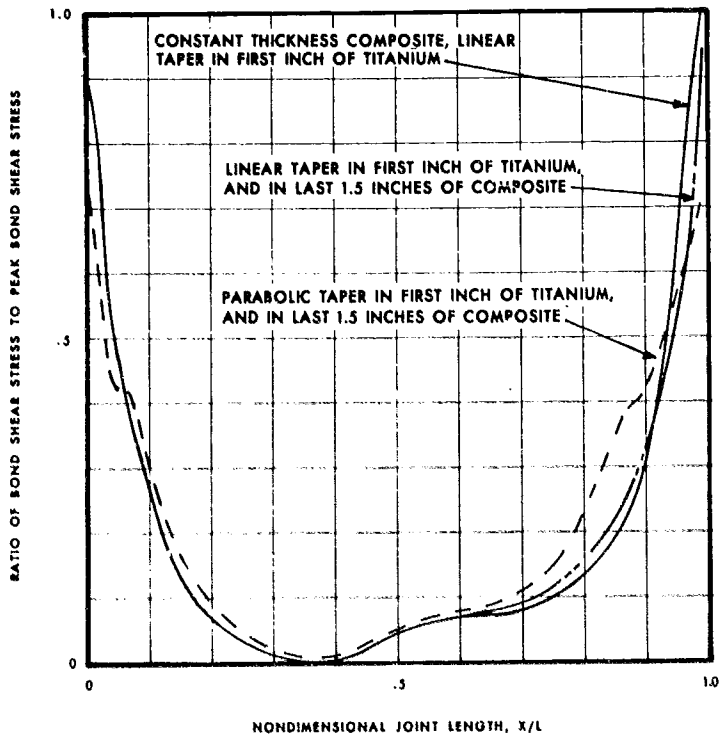


FIGURE 45. BOND SHEAR STRESS DISTRIBUTIONS FOR VARIOUS TIP CONFIGURATIONS.

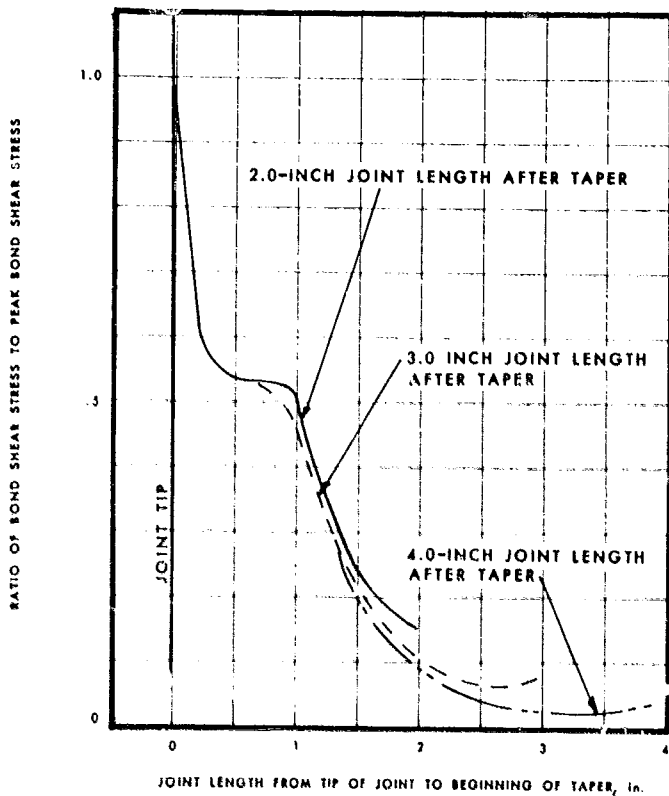


FIGURE 46. BOND SHEAR STRESS COMPARISON FOR VARIOUS JOINT LENGTHS AFTER TAPER.

A taper length of 1.5 inches was provided in the composite material since it was judged that a shorter taper could not be layed up with the required accuracy in the event that this taper would be as wound rather than machined. A longer taper length was also desired to accommodate the hoop windings which are discussed later on.

For the selected taper, the length of the bonded area between the taper in the titanium and the start of the incline in the fitting was varied. This was investigated to insure that this length was long enough to allow the shearing stresses in the bond to decrease before the incline was reached where high local bond tension loads were expected due to the composite fibers changing direction at the incline. Some of the results are shown in Figure 46. A 2.0-inch length was found to reduce the bond stress at the beginning of the incline to 15 percent of the peak value. Though longer lengths produced even lower shear stresses at the incline the 2.0-inch length was judged to be optimum from a weight-stress tradeoff standpoint.

To obtain better insight into the true stress distribution in the attachment area, a two-dimensional finite element analysis was performed on the joint using the preliminary design accomplished with the one-dimensional analysis. In this analysis both the graphite and titanium materials were modeled using quadrilateral orthotropic membrane elements. With the additional state of stress capability, the effect of the taper on the stress distribution could be investigated.

In this model the flexibility of bond line was not included, since the number of elements of reasonable aspect ratio required to represent this thin material would exceed the capacity of the program (1000 elements). The finite-element model is shown in Figure 47.

A comparison was made of the shear stresses at the bond line as calculated by this program and by the bond joint program. This was accomplished by using the stresses in the elements closest to the interface between the composite and the titanium. The shear stresses in the plane of the bond joint were obtained by rotating the stresses in the x-y plane using the conventional Mohr's circle formula.

$$\sigma_{x'x'} = \sigma_{xx} \cos^2 \theta + \sigma_{yy} \sin^2 \theta + 2\tau_{xy} \sin \theta \cos \theta$$

$$\sigma_{y'y'} = \sigma_{yy} \cos^2 \theta + \sigma_{xx} \sin^2 \theta - 2\tau_{xy} \sin \theta \cos \theta$$

$$\tau_{x'y'} = (\sigma_{yy} - \sigma_{xx}) \sin \theta \cos \theta + \tau_{xy} (\cos^2 \theta - \sin^2 \theta)$$

The comparison is shown in Figure 48. At the extremities of the joint, the peak shear stress distributions are similar.

Correlation of the two analyses was expected in this zone of the structure since the state of stress is primarily one dimensional away from the inclined region. The lack of bond line flexibility in the finite-element analyses should result in a slight overprediction of the bond line shear stresses.

The good correlation in the areas of the critical bond stresses gave confidence to the fact that the design decision made using the bonded joint analysis program was valid.

The effect of the incline on the stress distribution is also of concern. At both ends of the inclined area the fibers change direction, causing a complicated stress situation in the composite material. Also the compression stresses and corresponding shear reactions imposed by the incline were of concern. To study this situation, the joint was analyzed for various incline angles. The bond shear stress along the joint is shown for various incline angles in Figure 49. In order to maintain a reasonable bonding area at the root end of the joint, the length of the incline for the 20° incline was shortened, and both the root end and outboard diameters were maintained at the same value as the 10° inclines. The root end diameter of the 5° incline was increased while maintaining the same outboard diameter as for the 10° and 20° incline. The analysis indicates that a 20° incline would be unacceptable since the bond shear stress level approaches ± 2500 psi, which is attributed to both the rotation of the stresses through such a large angle and the short length of the inclined portion of the joint. Although the 5° incline produces the lowest bond shear stresses, it was felt that a 5° incline would not provide enough of a mechanical lock in the event of a bond failure. The 10° incline was therefore selected.

The design includes windings at 90 degrees to the span (hoop windings) over the basic composite structure in the area of the incline. These provide the hoop stiffness required to provide a mechanical lock along the incline in the event of a bond failure. The windings were sized for hoop stresses due to the wedging action which occurs on the incline with a bond failure.

To solve for the hoop winding thickness required, the ultimate centrifugal force was applied to the spar and reacted by pressure and friction components along the incline. The pressure distribution was assumed to be linear, being maximum at the outboard end of the incline, the coefficient of static friction between the composite and titanium was conservatively taken as .25. (Figure 50 presents the model used for determining the hoop stress).

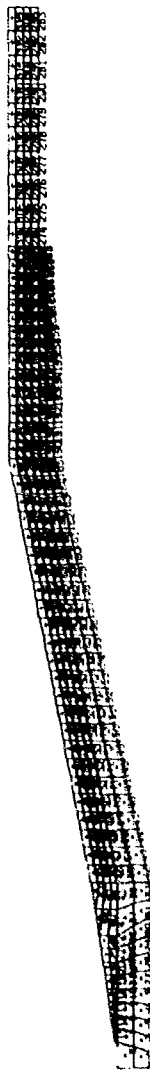


FIGURE 47. FINITE-ELEMENT MODEL.

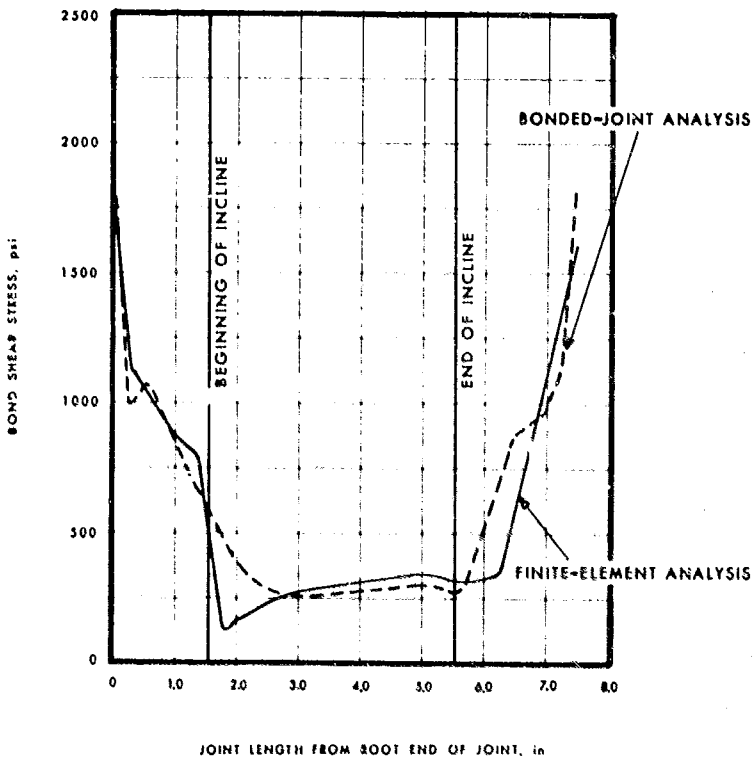


FIGURE 48. CORRELATION OF BOND SHEAR STRESS LEVELS FOR FINITE-ELEMENT AND BONDED-JOINT ANALYSIS.

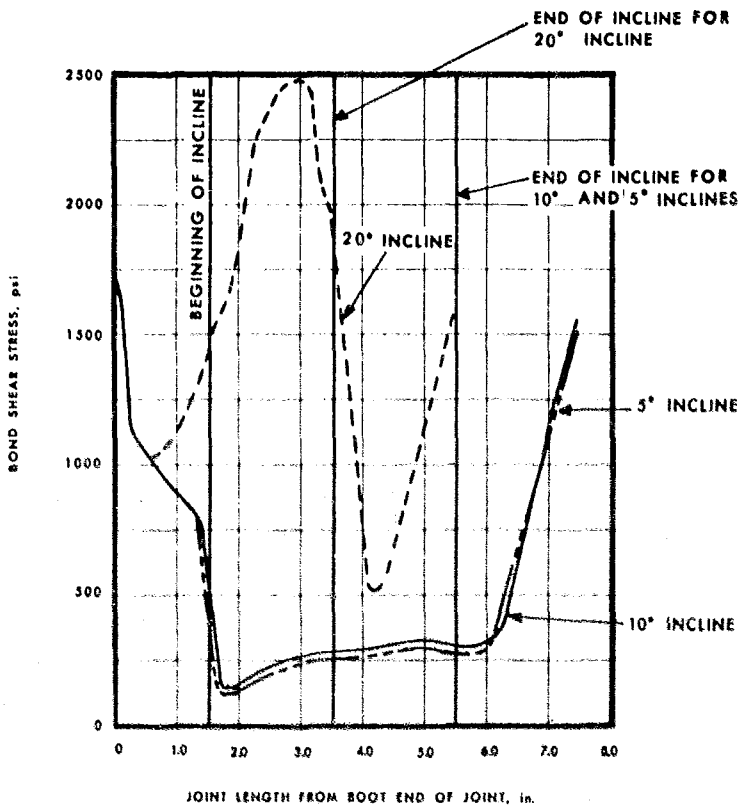


FIGURE 49. BOND SHEAR STRESS FOR VARIOUS INCLINE ANGLES.

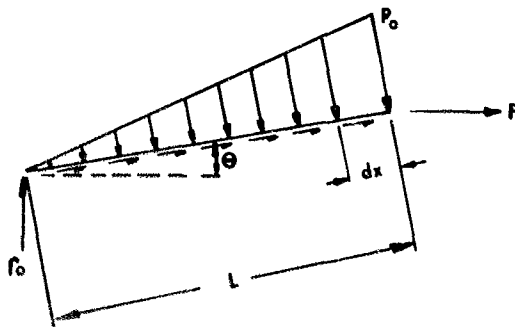


FIGURE 50. MODEL FOR DETERMINING HOOP WINDING.

The spar being relatively soft in the hoop direction, was assumed to react none of the pressure in hoop tension, so the hoop winding alone was sized to react the pressure forces in hoop tension. Under these assumptions the thickness required for the 90-degree windings at the critical outboard end was solved for by the formula

$$df = Pr^2 \pi \sin \theta \, dx + \mu P^2 \pi r \cos \theta \, dx$$

$$F = 2 \pi \int Pr (\sin \theta + \mu \cos \theta) \, dx$$

$$r = r_o + \Delta r x$$

$$P = P_o \frac{x}{L}$$

$$F = \frac{2 \pi (\sin \theta + \mu \cos \theta) P_o}{L} \int_0^L (r_o x + \Delta r x^2) dx$$

$$F = 2 \pi (\sin \theta + \mu \cos \theta) P_o \left[ \frac{r_o L}{2} + \frac{\Delta r L^2}{3} \right]$$

$$L = 4.06 \text{ in.}$$

$$r_o = 3.65 \text{ in.}$$

$$\Delta r = .70 \text{ in.}$$

$$F = F_c \text{ ultimate} = 1.5 (F_c \text{ limit}) = 102,000 \text{ lb}$$

$$\mu = .25$$

$$\theta = 10^\circ$$

Solving for  $P_o$ ,

$$P_o = 3426 \text{ psi} \tag{21}$$

$$\sigma_{\text{Hoop}} = \frac{PR}{t}$$

$$t = \frac{P_o R}{\sigma_{\text{Hoop allowable}}}$$

$$t = \frac{3426 (4.35)}{140,630}$$

$$t = .106 \text{ in.}$$

The thickness was used over the full length of the incline with appropriate tapering at both extremities.

The axial vibratory stress levels in the titanium and the composite in the joint area are shown in Figure 51. The fatigue margins of safety were calculated for the peak stresses in the joint. In the composite component of the joint, the peak vibratory stress is 11,000 psi. The margin of safety was calculated to be

$$MS = \frac{\sigma_{\text{allow}}}{\sigma_{\text{peak}}} = 1.0$$

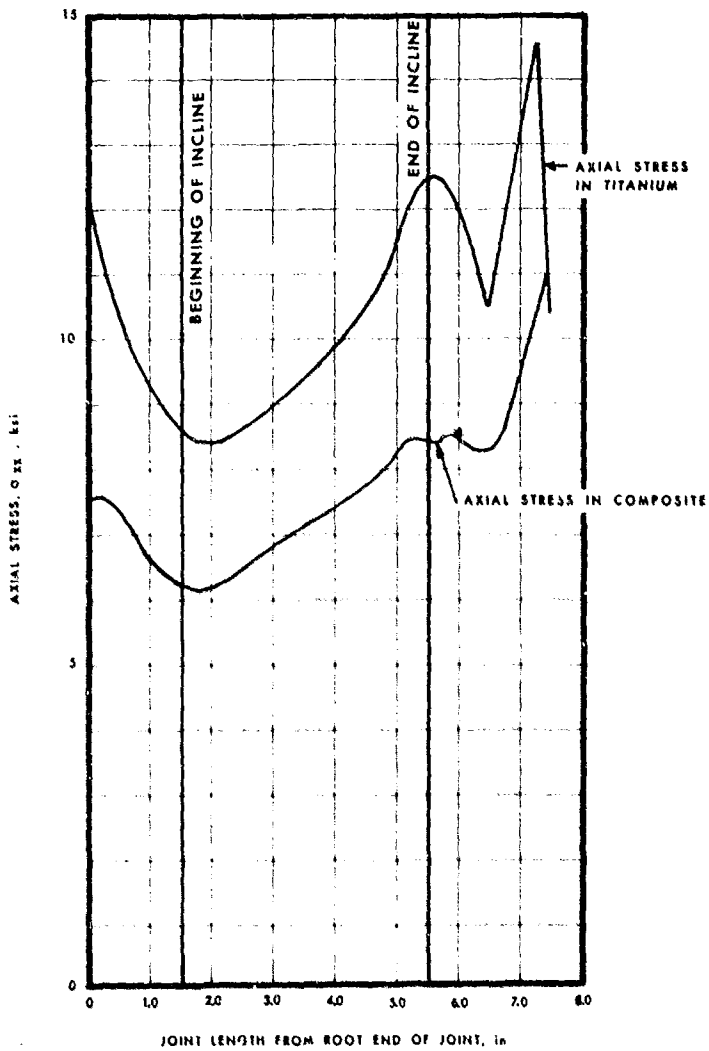


FIGURE 51. VIBRATORY AXIAL STRESS IN BONDED JOINT.

where  $\sigma_{\text{allow}}$  = the allowable fatigue stress for the composite material

$$\sigma_{\text{allow}} = (\epsilon_{\text{composite}}) (\epsilon_{\text{All composite}})$$

$$\sigma_{\text{allow}} = (12.27 \times 10^6 \text{ lb/in.}^2) (\pm 13,000 \text{ in./in.})$$

$$\sigma_{\text{allow}} = \pm 15,951 \text{ psi}$$

$$\text{MS} = \frac{\pm 15,951}{\pm 11,100} - 1.0$$

$$\text{MS} = + .439$$

In the titanium component of the joint the peak vibratory stress is  $\pm 14,600$  psi. Using equation 20, the working vibratory stress level for  $\beta$ -STOA titanium is  $\pm 65,000$  psi. The allowable vibratory stress in this region of the bonded joint was established.

where  $K_S$  = surface finish factor = 1.25

$K_F$  = fatigue strength reduction factor = 1.25

$F_R$  = reliability factor = .70

$F_{SE}$  = size effect factor = .72

$$\sigma_{\text{vallow}} = \frac{\pm 65,000}{1.25 (1.25)} (.70) (.72)$$

$$\sigma_{\text{vallow}} = \pm 20,900 \text{ psi}$$

The resulting margin of safety was established to be

$$\text{MS} = \frac{\sigma_{\text{vallow}}}{\sigma_{\text{v peak}}} - 1.0$$

$$\text{MS} = \frac{\pm 20,900}{\pm 14,600} - 1.0$$

$$\text{MS} = +.431$$

#### TITANIUM BACKUP STRUCTURE

Inboard of the bonded joint, the titanium fitting is required to carry all of the load. The primary area of concern in the titanium fitting is directly inboard of the joint end where the fitting flairs up into the bearing retention portion of the joint. Although there is a generous radius in this section, there is a stress concentration associated with it.

The stress concentration factor was established using a theoretical model similar to the configuration of the titanium fitting, Figure 52.

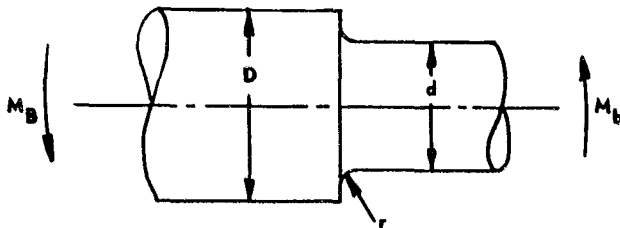


FIGURE 52. THEORETICAL MODEL OF JOINT FOR STRESS CONCENTRATION FACTOR.

Using Figure 53 and the values of

$$\begin{aligned} r &= 1.5 \text{ in.} \\ d &= 6.50 \text{ in.} \\ D &= 10.75 \text{ in.} \end{aligned}$$

the theoretical stress concentration factor was determined to be  $K_t = 1.56$ .

The fatigue margin of safety was determined using fatigue stress allowables derived from equation (20). The working fatigue stress at  $10^8$  cycles for  $\beta$ -STOA titanium is  $\pm 65,000$  psi. The allowable vibratory stress is a function of the stress concentration factor, surface finish factor, reliability, and size effect factors. Using equation 20 and the values of  $K_f$ ,  $K_s$ , and  $F_{SE}$  given below, the allowable vibratory stress is

$$K_f = 1.38$$

$$K_s = 1.25$$

$$F_B = .70$$

$$F_{SE} = .72$$

$$\sigma_v \text{ allow} = \frac{\pm 65,000 \text{ psi}}{1.38 (1.25)} (.70) (.72)$$

$$\sigma_v \text{ allow} = \pm 19,000 \text{ psi}$$

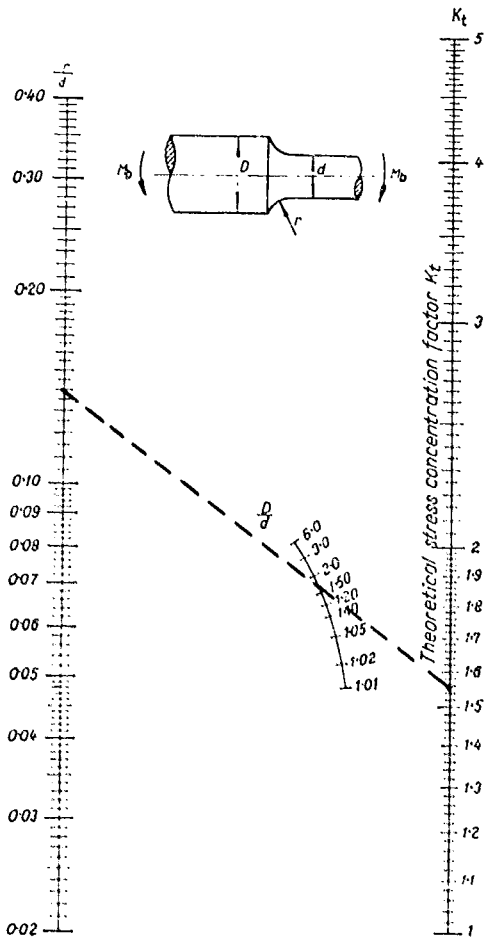


FIGURE 53. THEORETICAL STRESS CONCENTRATION FACTOR FOR TITANIUM FITTING.

The vibratory stress due to combined flapwise and edgewise bending at that section is

$$\sigma_v = \frac{M_v R}{I}$$

$$\sigma_v = \frac{(\pm 255,000) (3.65)}{51.8}$$

$$\sigma_v = \pm 18,000 \text{ psi}$$

The vibratory margin of safety then becomes

$$MS = \frac{\sigma_v \text{ allow}}{\sigma_v} - 1.0$$

$$MS = \frac{\pm 19,000}{\pm 18,000} - 1.0$$

$$MS = + .055 \text{ at } 10^8 \text{ cycles}$$

The flanges in the bearing retention segment of the titanium fitting were analyzed using a finite-element analysis (Program F768). The thickness of the flange, main backup structure, and fillet radius was determined by varying the parameters shown in Figure 54 and establishing the configuration which produced the lowest stress level in the radius.

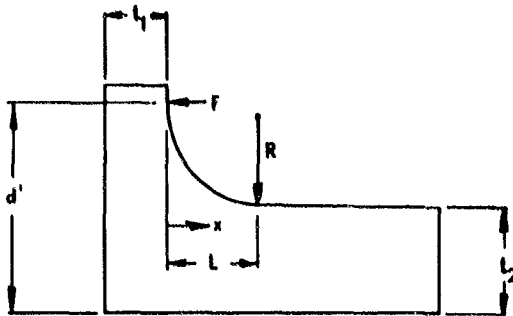


FIGURE 54. FLANGE LOADING.

The load was applied to the flange as shown in Figure 54 to simulate a preload due to the bearings. The configurations investigated are summarized in Table 7. Four of the configurations are for a compound radius, and one is for a single radius. The results are shown in Figure 55.

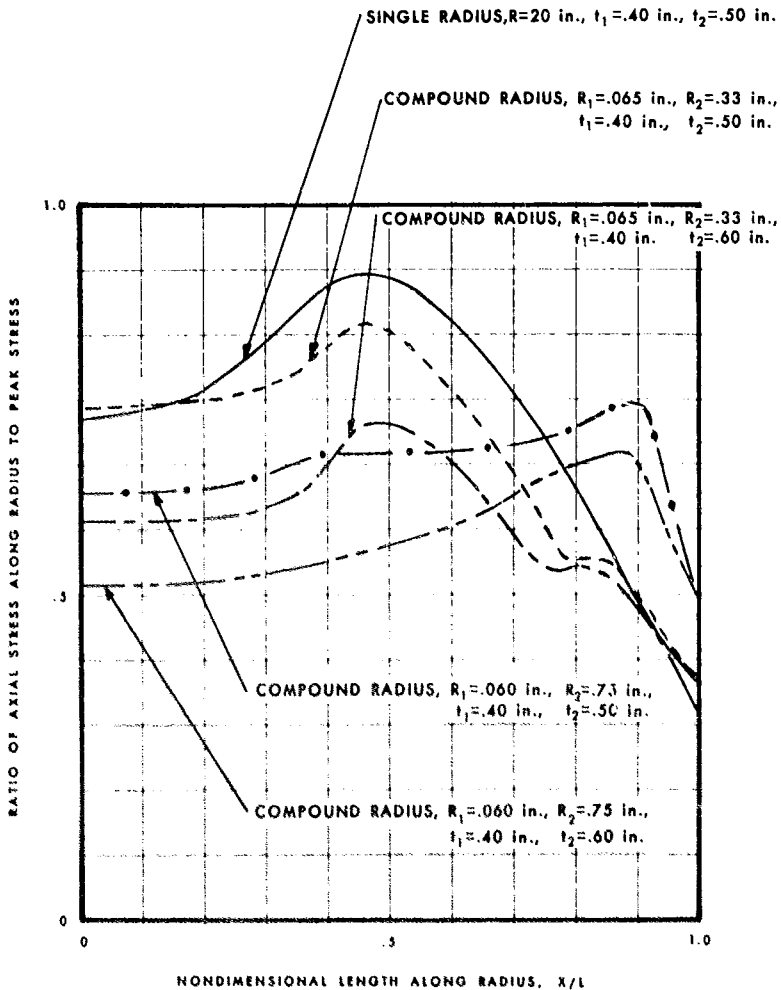


FIGURE 55. RELATIVE AXIAL STRESS LEVELS ALONG THE RADIUS OF THE BEARING RETENTION FLANGE OF VARIOUS GEOMETRIES.

TABLE 7. CONFIGURATIONS INVESTIGATED IN TITANIUM BEARING RETENTION FLANGE ANALYSIS

Case	$t_1$	$t_2$	$R_1$	$R_2$	R
1	.4	.5	-	-	.20
2	.4	.5	.065	.33	-
3	.4	.6	.065	.33	-
4	.4	.5	.060	.75	-
5	.4	.6	.060	.75	-

The results indicate that case 5 produces the lowest stress level. Therefore, the dimensions of case 5 were used for the titanium fitting in the bearing retention segment of the root end fitting.

The allowable vibratory stress was calculated using equation 20. The stress concentration factor for the configuration used was determined by

$$K_t = \frac{\sigma_{\max}}{\sigma_{\text{nom}}} \quad (23)$$

The value of  $\sigma_{\max}$  was established by the finite element analysis. The nominal stress,  $\sigma_{\text{nom}}$ , was established by the applied load. Due to the position of the applied load a moment is produced in the radius section of the flange. The nominal stress was calculated as

$$\sigma_{\text{nom}} = \frac{F}{A} + \frac{Mc}{I} \quad (24)$$

$$\text{For constant cross-section } \frac{Mc}{I} = \frac{6M}{t^2}$$

$$\sigma_{\text{nom}} = \frac{F}{A} + \frac{6M}{t_2^2}$$

$$M = F \left( d' - \frac{t_2}{2} \right)$$

For a 1-inch thick section  $A = t_2$

$$\sigma_{\text{nom}} = \frac{F}{t_2} \left[ 1 + \frac{6 \left( d' - \frac{t_2}{2} \right)}{t_2} \right]$$

The resulting stress concentration factor was

$$K_t = 1.63$$

The surface finish factor, reliability, and size effect factors were the same as those used in the analysis of the section directly inboard of the point end. Using equation 20, the resulting allowable vibratory stress was calculated to be

$$\sigma_v \text{ allow} = \frac{\pm 65,000 \text{ psi}}{1.45 (1.25)} (.7) (.72)$$

$$\sigma_v \text{ allow} = \pm 18,000 \text{ psi}$$

The vibratory stress level due to combined flapwise and edgewise bending was determined to be

$$\sigma_v = \frac{MR}{I}$$

$$\sigma_v = \frac{(\pm 255,000) (5.10)}{209.}$$

$$\sigma_v = \pm 6,200 \text{ psi}$$

The resulting margin of safety was calculated to be

$$MS = \frac{\sigma_v \text{ allow}}{\sigma_v} - 1.0$$

$$MS = + 1.90$$

### LAP SHEAR TESTS

To evaluate shear allowables for the bond between the titanium fitting and the graphite epoxy spar, static tests were performed on a number of lap shear specimens. The configuration of the joint is as shown in Figure 56. The composite material constituting the upper and lower adherend was configured from the same fiber lay-up and resin system that was used in the design of the spar. Specimens were configured with and without the addition of adhesive to the joint to determine the shear strength of the epoxy resin in bonding relative to that of the adhesive bond.

A total of 22 lap shear joints were pulled in a tensile test machine similar to the one shown in Figure 57. Nineteen of these lap joints did not include a bond line, since it was desired to investigate the static shear strength of the composite resin system as a bond. The remaining 3 lap joints included a .006-in.-thick Hysol 9602.3 adhesive cured at 250°F for 1 hour with 20 psi pressure.

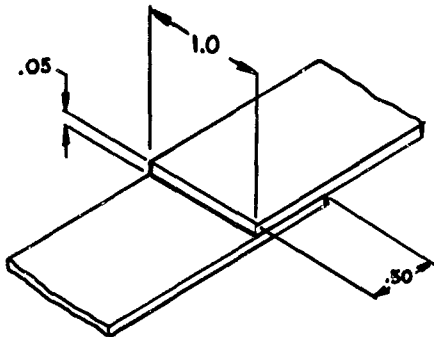


**FIGURE 56 . GEOMETRY OF LAP SHEAR SPECIMENS.**

The shear stress was evaluated by using Sikorsky Aircraft's bonded joint analysis computer program (Y004<sup>B</sup>). The joint was modeled by assuming a bond line of .001 inch and applying a direct axial stress to the model. The results provide a shear stress distribution along the joint, as well as the direct axial stress. In order to establish a bond shear stress level, the analysis was performed using a bond line of .006 inch. A direct axial stress of 2000 psi was applied to the model, and the resulting shear stress levels for both a bonded and a nonbonded joint are shown in Figure 58.

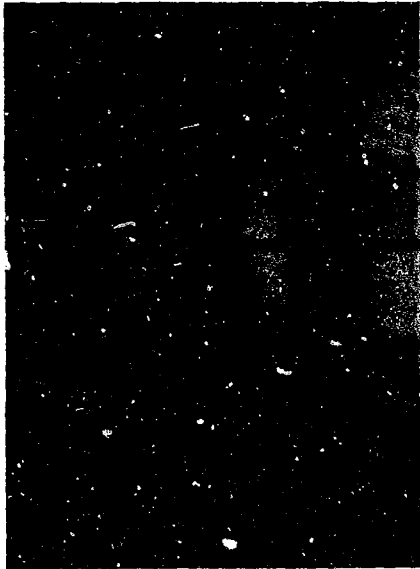


FIGURE 57. TESTING OF LAP SHEAR SPECIMENS.

From the computer analysis, a ratio of the peak stress in the joint to the axial stress was determined for the two configurations. Then the peak shear stress for each test specimen was determined by multiplying these ratios by the specimen axial stress at failure.

$$\tau_{\text{peak test}} = \left( \frac{\tau_{\text{Peak}}}{\sigma} \right) \sigma_{\text{test at failure}} \quad (25)$$

where

$$\sigma_{\text{test at failure}} = \frac{F_{\text{Test at Failure}}}{A}$$

A = cross-sectional area of joint adherends

A = .050 in.<sup>2</sup>

$$\frac{\tau_{\text{peak}}}{\sigma} = .224 \quad (\text{with bond})$$

$$\frac{\tau_{\text{peak}}}{\sigma} = .351 \quad (\text{no bond})$$

Table 8 presents the results of the static lap shear tests for the non-bonded specimens. The results indicate that for a specimen having only the resin system as a bond, the shear strength of the resin, as a bond, is between 4,000 and 9,000 psi.

Table 9 presents the results of the static lap shear tests for the bonded specimens. The results indicate that for a specimen having a bond of .006 inch thickness, no increase in predicted peak shear was obtained. From Figure 58 this is in accordance with predicted results.

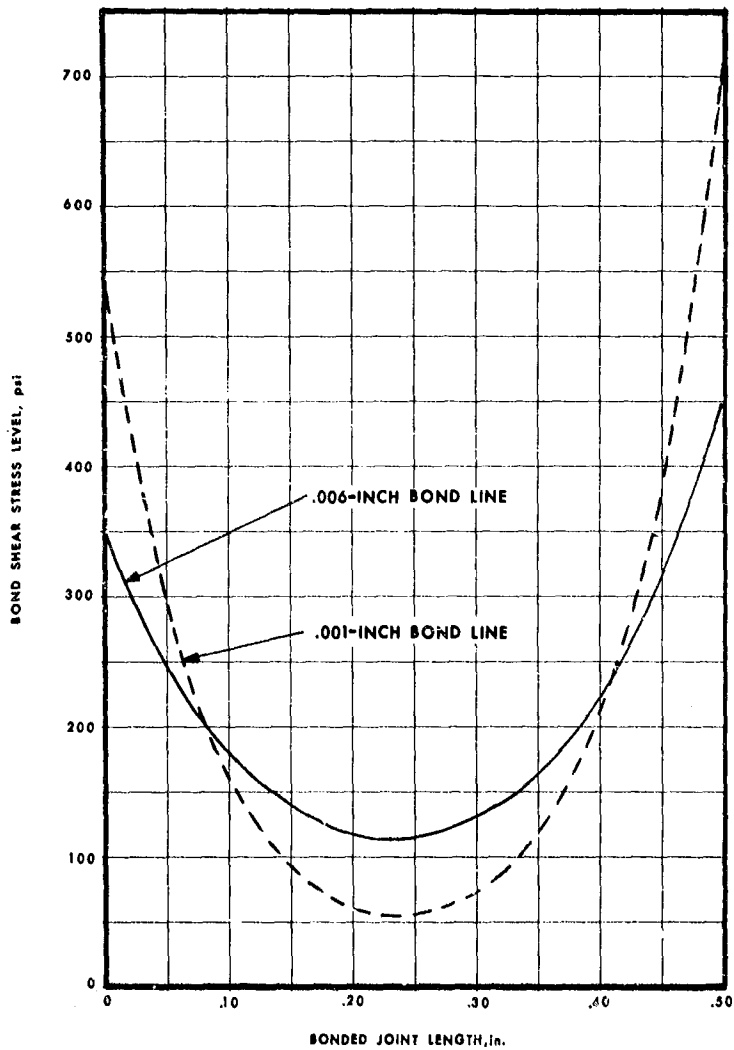


FIGURE 58. BOND SHEAR STRESS FOR LAP SHEAR TENSILE TEST MODEL.

TABLE 8. NONBONDED LAP SHEAR TEST RESULTS

Specimen	Failure Load (lb)	Direct Axial Stress (psi)	Predicted Shear Stress (psi)
1	754	15,080	5,286
2	650	13,000	4,557
3	744	14,880	5,215
4	622	12,446	4,360
5	1,168	23,360	8,188
6	1,224	24,480	8,580
7	900	18,000	6,309
8	1,236	24,720	8,664
9	760	15,200	5,328
10	1,060	21,200	7,431
11	1,216	24,320	8,524
12	1,028	20,560	7,206
13	682	13,640	4,780
14	1,152	23,040	8,076
15	1,208	24,160	8,468
16	1,288	25,760	9,028
17	918	18,360	6,435
18	942	18,840	6,603
19	1,256	25,120	8,805

TABLE 9. BONDED LAP SHEAR TEST RESULTS

Specimen	Failure Load (lb)	Direct Axial Stress (psi)	Predicted Shear Stress (psi)
1	1,186	23,720	5,313
2	1,198	23,960	5,367
3	1,476	29,520	6,612

### TRADE-OFF STUDIES

The objective of the trade-off studies conducted was to establish the relative merits of the three configurations:

Filament-Wound Spar Design  
Twin Beam Design  
Conventional Design

In the cost studies, the rate used to determine labor cost was \$16.00 per hour. The cost of filament winding graphite material was based upon \$20.00 per pound, and the cost of prepreg graphite materials was based upon \$25.00 per pound. These are projected costs for the 1980 time frame based upon the best predictions available.

No attempt was made to amortize the nonrecurring costs associated with any of the configurations. It was assumed that the major nonrecurring cost items of design, tooling and test would be approximately the same for the three designs and would not therefore change the relative positions. This assumption was based upon the expectation that regardless of the details of the construction of a main rotor blade, these costs are relative to the size and performance requirements of the blade.

The learning curve used for the labor content of the three configurations was 85%. The choice of this curve was based upon past experience on this type of component. The cumulative average learning curve was based upon the following equation:

$$Y = CX^{-N}$$

where Y = Unit hours  
C = First unit hours  
X = Unit quantity  
N = Slope determinate

For an 85% learning curve  $N = .2345$ .

No learning curve rationale was placed upon the material costs for any of the configurations.

#### FILAMENT-WOUND SPAR DESIGN COSTS

The manufacturing processes and material costs for this configuration are identical to the demonstrator design with the exception of the spar.

The filament-wound spar costs were based upon the following estimates:

There is 40 lb of graphite material at \$20/lb in the spar, amounting to \$800. Other material costs, adhesives and tip end fittings but not including the root end fitting, amount to an additional \$190. Labor costs after 200 units average 58 hours per spar. The machining and integration of the root end fitting are estimated at 20 hours at the same quantities. Material cost is \$200. Putting the labor cost for the spar on an 85% learning curve gives the first unit labor hours @  $58 \times 200 \cdot 2345 = 201$  hours.

Converting this at the labor rate of \$16/hour gives  $201 \times 16 = \$3216$ .

The remainder of the blade and material costs are the same as for the demonstrator. The  $T_1$  labor cost for this portion is \$35,536 plus a material cost of \$4,000.

Summarizing the  $T_1$  costs for the filament-wound blade:

(1) Labor cost excluding spar	\$35,536
(2) Spar labor cost	3,216
(3) Spar material Cost	1,190
(4) Other material cost	<u>4,000</u>
	\$43,942

(1) and (2) are subject to the learning curve progression at 85%.

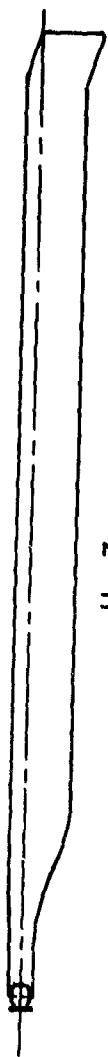
The cumulative average cost for quantities of 200, 500, 1000 and 2000 units, using an 85% learning progression for the labor costs and leaving material costs constant, is as follows:

	<u>200</u>	<u>500</u>	<u>1000</u>	<u>2000</u>
(1) $35,536 \div \text{Unit Qty.}^{.2345}$	10,258	8,275	7,033	5,978
(2) $3216 \div \text{Unit Qty.}^{.2345}$	928	749	636	541
(3) 1190	1,190	1,190	1,190	1,190
(4) 4000	<u>4,000</u>	<u>4,000</u>	<u>4,000</u>	<u>4,000</u>
Totals	\$16,376	\$14,214	\$12,859	\$11,709

#### TWIN-BEAM DESIGN COSTS

The approach taken on this cost study was to scale down the elements of the Sikorsky H-3 composite blade in accordance with the appropriate sizing factors. Figure 59 shows the comparative size of the H-3 blade and the ABC<sup>TM</sup> blade. The H-3 blade weight is 234 pounds compared to the ABC composite blade weight of 180 pounds. The blade lengths and chords respectively are (H-3) 334 in. and 22.75 in. (ABC<sup>TM</sup> 212 and 16 in. average).

From the latest design-to-cost studies on the H-3 design, the average cost for 11 units is 1,214 hours plus \$9,392 for material. The material cost includes 64.6 pounds of prepreg graphite at \$68 per pound.



H - 3



ABC

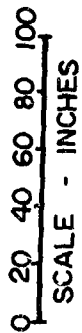


FIGURE 59. ABC TO H-3 SIZE COMPARISON.

To normalize the material costs to 1980 values, the material would be  $9392 - (64.6 \times 68) + 64.6 \times 25 = \$6614.2$ .

To normalize the labor cost to the first unit cost using an 85% learning curve gives  $1214 \times 11.2345 = 2130$  hours.

The materials used in the H-3 blade are the same type of material used in the ABC twin-beam design. These materials are prepreg graphite, prepreg fiberglass and honeycomb core. On this basis the material costs may be scaled by weight. The ABC cost of material is therefore  $\frac{180}{234} \times 6614 = \$5087$ .

The labor hours involved in the lay-up, curing and machining of the H-3 twin-beam design are directly related to the planform area of the blade. The number of plies of material laid up are very similar. The ABC blade, however, introduces a complexity due to the tapered planform and more significant tapering of thickness. To allow for this complexity a factor of 2 to 1 is added to the labor hours after scaling by the areas of the H-3 and ABC blades. This scaling and factoring produces labor costs of

$$2 \times \frac{212 \times 16}{334 \times 22.75} \times 2130 \times \$16 = \$30,426$$

The summary of  $T_1$  cost of the ABC blade is as follows:

- (1) Material \$ 5,087
- (2) Labor \$30,426

(2) is subject to an 85% learning curve progression.

The cumulative average cost for quantities of 200, 500, 1000 and 2000 units, using an 85% learning curve for the labor costs and leaving materials costs constant is as follows:

Quantity	200	500	1000	2000
(1) 5087	5,087	5,087	5,087	5,087
(2) 30,426 ÷ Unit Qty. <sup>.2345</sup>	8,783	7,085	6,022	5,119
	\$13,870	\$12,172	\$11,109	\$10,206

#### DEMONSTRATOR BLADE COST

Twenty blades were fabricated plus two fatigue specimens. When the cost of the fatigue specimens was subtracted from the total cost, it was found that the blade average cost amounts to 1100 labor hours plus \$25,714 material cost, which includes the subcontract labor involved in the fabrication of the spar. The total titanium spar cost in the demonstrator was \$21,704. The raw material cost contained in this spar was \$14,695, leaving \$7019 which is subject to the learning curve progression.

Summarizing the demonstrator cost, for the average of 20 blades:

(1) Rotor hours	1100
(2) Subcontract spar labor cost	\$ 7,019
(3) Spar material cost	\$14,695
(4) Other material cost	\$ 4,000

(1) and (2) are subject to the learning curve progression at 85%. These values projected back to the first theoretical unit ( $T_1$ ) become:

$$(1) 1100 \times 20^{-.2345} = 2221 \text{ hours}$$

$$(2) \$7,019 \times 20^{-.2345} = \$14,169$$

Converting labor hours to dollars at the rate of \$16/hour, the total  $T_1$  cost of the demonstrator blade becomes:

(1) 2221 x 16	= \$35,536
(2)	14,169
(3)	14,695
(4)	4,000
	<hr/>
	\$68,400

The cumulative average cost for quantities of 200, 500, 1000 and 2000 units, using an 85% learning curve progression for the labor costs and leaving material costs constant, is as follows:

<u>Quantity</u>		<u>200</u>	<u>500</u>	<u>1000</u>	<u>2000</u>
(1) 35536 ÷ Unit Qty. $\cdot 2345$	=	10,258	8,275	7,033	5,978
(2) 7019 ÷ Unit Qty. $\cdot 2345$	=	2,026	1,634	1,389	1,181
(3) 14,695	=	14,695	14,695	14,695	14,695
(4) 4000	=	4,000	4,000	4,000	4,000
		<hr/>	<hr/>	<hr/>	<hr/>
Totals		\$30,979	\$28,604	\$27,117	\$25,854

#### SUMMARY OF COST TRADE-OFFS

Quantities	<u>200</u>	<u>500</u>	<u>1000</u>	<u>2000</u>
(a) Filament-wound spar design	\$16,376	\$14,214	\$12,853	\$11,709
(b) Twin-beam design	\$13,870	\$12,172	\$11,109	\$10,206
(c) Conventional Design	\$30,979	\$28,604	\$27,117	\$25,854

Within the accuracy obtainable with long-range projection of costs, the two all-composite designs cost the same. The conventional design, due to the high cost of spar fabrication, costs the most to produce.

It should be noted that these cost comparisons reflect only the comparative costs and do not include factors for general administration, profit, or other items which are considered to be equal for all configurations. It was not considered possible to rationalize whether any of the designs would have a higher or lower rejection rate than the other; therefore, it was assumed that this factor would be equal for all configurations.

#### SPAR WEIGHT SUMMARY

Figure 60 illustrates the weight distribution along the spar of both composite spar designs and the titanium demonstrator spars. The effect of the modified root pitch bearing configuration has been removed from the three designs since this is applicable to all in a similar manner. Spar material densities used were .07 pound per cubic inch for the graphite epoxy and .16 pound per cubic inch for titanium.

Comparing a demonstrator spar weight of 97.7 pounds from station 15 outboard to the tip, both composite spar equivalents have a weight of 60.6 pounds, giving a delta weight reduction of 37.1 pounds.

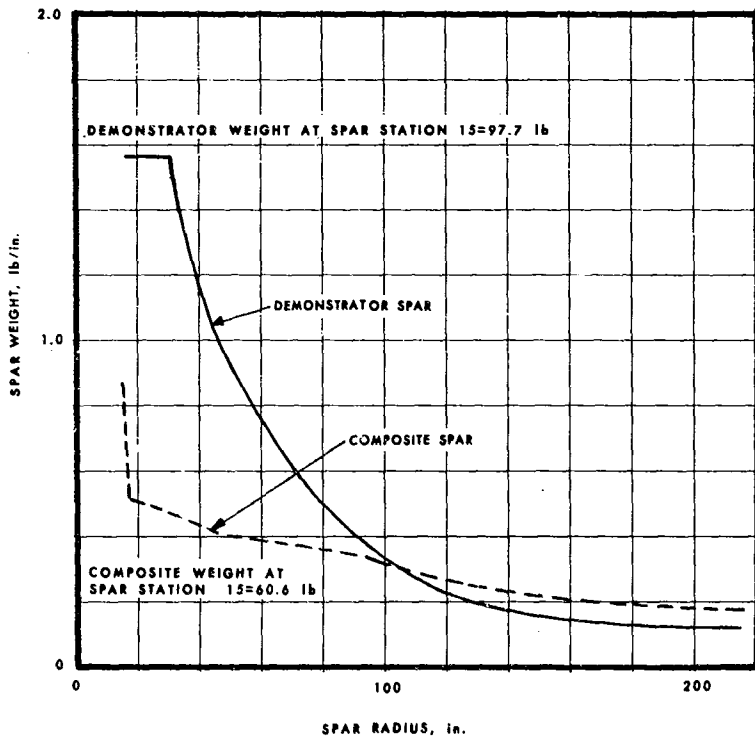


FIGURE 60. SPAR WEIGHT DISTRIBUTION FOR COMPOSITE AND DEMONSTRATOR SPARS.

## CONCLUSIONS

1. Filament winding can be applied to the design and fabrication of a tapered planform and varying thickness spar of a main rotor blade to the ABC™ requirements.
2. These are some manufacturing limitations and risks associated with this design approach.
  - . One of the manufacturing limitations is the inability to obtain a  $0^\circ$  winding angle without compromising producibility. The  $15^\circ$  minimum winding angle which can be economically obtained results in a slight compromise in weight.
  - . Another of the manufacturing limitations is the necessity to terminate the fiber plies at spanwise locations to achieve the spanwise taper with controlled thickness. To reduce the number of terminations to acceptable limits, the thickness was allowed to grow a little above the optimum theoretical thickness. This conformance may be overcome in a production situation with the application of a fully automated winding machine in which the terminations are made by machine rather than by hand as planned for prototype fabrication.
  - . One of the fabrication risks is associated with making the prototype ply terminations by hand. The technique of making a termination involves stopping the winding operation and cutting the filaments at the required locations. On a small number of terminations, this procedure is not too difficult. The risk becomes progressively higher as the number of terminations increases. This difficulty would be overcome in production by automating this operation.
  - . Another fabrication risk is the integration of the root end fitting. The configuration selected was shown by analysis to be a low-weight solution but requires that the filaments be machined or hand trimmed to a specific shape after the winding operation. It also requires a supplementary operation during the winding to obviate the slipping of fibers at the turnaround for the end of each layer before starting another winding layer.
  - . The repeatability of filament winding must be demonstrated on a number of spars before it can be determined that the mass moments between spars can be fabricated within the limits acceptable to produce interchangeable blades.
  - . The process of post forming from the round shape to the elliptical spar shape may be expected to produce a porous laminate at the leading and trailing edges. If it is determined that the quality obtained by this method is unacceptable, the solution would lie in winding over a rigid split mandrel close to the final shape of the spar.

3. Cost and weight differences between the filament winding design and the open-mold composite H-3 design are small. However, both composite designs show a dramatic cost and weight improvement over the conventional titanium demonstrator blade.
  - . Both composite designs show a delta weight saving of 37 pounds in a spar which weighs 97.7 pounds, a percentage weight reduction of 37.8%.
  - . The cost reduction of both composite designs shows a cost saving of 50% and more in the production cost projections.
4. The feasibility of a filament-wound design to meet the ABC<sup>TM</sup> design requirements, and to be fabricated with cost and weight advantages, was established by this study.

#### RECOMMENDATIONS

1. This program should be followed by a risk reduction fabrication phase to optimize the root end fitting integration and ply terminations techniques.
2. Fatigue tests should be conducted on full-scale specimens to verify the quality of laminate obtained by the filament winding process on a heavy-walled spar.

REFERENCE

1. Sors, L., Fatigue Design of Machine Components, Toronto, Sydney, Braunschweig, Pergamon Press, 1971, P. 70.

LIST OF SYMBOLS

A	cross-sectional area, in. <sup>2</sup>
A'	mean enclosed area, in. <sup>2</sup>
AE	axial stiffness, lb
CF	centrifugal force, lb
C <sub>D</sub>	edgewise distance from neutral axis of blade to point of stress calculation, in.
C <sub>F</sub>	flapwise distance from neutral axis of blade to point of stress calculation, in.
D	outside tube diameter, in.
d	inside tube diameter, in.
d'	reference distance, in.
E	elastic modulus, psi
EI <sub>xx</sub>	flapwise stiffness, lb-in. <sup>2</sup>
EI <sub>yy</sub>	edgewise stiffness, lb-in. <sup>2</sup>
F	applied load, lb
F <sub>R</sub>	reliability factor
F <sub>SE</sub>	size effect factor
G	shear modulus, psi
GJ	torsional stiffness, lb-in. <sup>2</sup>
I	moment of inertia of cross-sectional area, in. <sup>4</sup>
J	polar moment of inertia, in. <sup>4</sup>
K <sub>f</sub>	fatigue strength reduction factor
K <sub>s</sub>	surface finish factor
K <sub>t</sub>	stress concentration factor
L	length, in.
M	combined flapwise and edgewise bending moments, in.-lb

$M_E$  edgewise bending moment, in.-lb  
 $M_F$  flapwise bending moment, in.-lb  
 $M_T$  torsional moment, in.-lb  
 $N_{15}$  number of  $\pm 15^\circ$  plies  
 $N_{45}$  number of  $\pm 45^\circ$  plies  
 $P$  pressure load, psi  
 $P_0$  initial pressure load, psi  
 $R$  radius, in.  
 $r$  radius, in.  
 $r_0$  initial radius, in.  
 $t$  thickness, in.  
 $t_{act}$  actual thickness, in.  
 $t_n$  thickness per layer, in.  
 $t_{req}$  required thickness, in.  
 $t_{15}$  thickness of  $\pm 15^\circ$  plies, in.  
 $t_{45}$  thickness of  $\pm 45^\circ$  plies, in.  
 $U$  length of median boundary, in.  
 $X$  reference distance, in.  
 $\alpha_x$  ratio of flapwise composite blade stiffness to flapwise demonstrator blade stiffness,  $\frac{E_{Ixx} \text{ Composite}}{E_{Ixx} \text{ Demonstrator}}$   
 $\alpha_J$  ratio of torsional composite blade stiffness to torsional demonstrator blade stiffness,  $\frac{GJ \text{ Composite}}{GJ \text{ Demonstrator}}$   
 $\gamma$  shear strain,  $\mu\text{in./in.}$   
 $\gamma_{allow}$  allowable shear strain  $\mu\text{in./in.}$   
 $\Delta_r$  change in radius, in.  
 $\epsilon$  axial strain,  $\mu\text{in./in.}$   
 $\epsilon_{allow}$  allowable axial strain,  $\mu\text{in./in.}$

$\theta$	angle of orientation, deg.
$\mu_{l,i}$	coefficient of friction
$\mu$	damped model amplification factor
$\xi$	damping function
$\sigma$	stress, psi
$\sigma_{\text{allow}}$	allowable stress, psi
$\sigma_H$	hoop stress, psi
$\sigma_{\text{Hoop allow}}$	allowable hoop stress, psi
$\sigma_{\text{max}}$	maximum stress, psi
$\sigma_{\text{non}}$	nominal stress, psi
$\sigma_{\text{peak}}$	peak stress, psi
$\sigma_v$	vibratory stress psi
$\sigma_v \text{ allow}$	allowable vibratory stress, psi
$\sigma_v \text{ peak}$	peak vibratory stress, psi
$\sigma_{xx}$	axial stress, psi
$\sigma_{yy}$	transverse stress, psi
$\sigma_{x'x'}$	axial stress in a rotated coordinate system, psi
$\sigma_{y'y'}$	transverse stress in a rotated coordinate system, psi
$\tau_{\text{peak}}$	peak shear stress from computer analysis, psi
$\tau_{\text{peak test}}$	predicted peak shear stress from lap shear test, psi
$\tau_{xy}$	shear stress, psi
$\tau_{x'y'}$	shear stress in a rotated coordinate system, psi
$\phi$	phase angle, deg
$\Omega$	main rotor speed, rpm
$\omega$	natural frequency, cpm